Biophysical Journal
Article

Biophysical Society

TRPV4-dependent Ca^{2+} influx determines cholesterol dynamics at the plasma membrane

Yutaro Kuwashima,[1,2] Masataka Yanagawa,[2,3] Masashi Maekawa,[1,4] Mitsuhiro Abe,[2] Yasushi Sako,[2,*] and Makoto Arita[1,4,5,6,*]

[1]Division of Physiological Chemistry and Metabolism, Graduate School of Pharmaceutical Sciences, Keio University, Tokyo, Japan; [2]Cellular Informatics Laboratory, RIKEN Cluster for Pioneering Research (CPR), Saitama, Japan; [3]Molecular and Cellular Biochemistry, Graduate School of Pharmaceutical Sciences, Tohoku University, Sendai, Miyagi, Japan; [4]Laboratory for Metabolomics, RIKEN Center for Integrative Medical Sciences (IMS), Kanagawa, Japan; [5]Cellular and Molecular Epigenetics Laboratory, Graduate School of Medical Life Science, Yokohama City University, Kanagawa, Japan; and [6]Human Biology-Microbiome-Quantum Research Center (WPI-Bio2Q), Keio University, Tokyo, Japan

ABSTRACT The activities of the transient receptor potential vanilloid 4 (TRPV4), a Ca^{2+}-permeable nonselective cation channel, are controlled by its surrounding membrane lipids (e.g., cholesterol, phosphoinositides). The transmembrane region of TRPV4 contains a cholesterol recognition amino acid consensus (CRAC) motif and its inverted (CARC) motif located in the plasmalemmal cytosolic leaflet. TRPV4 localizes in caveolae, a bulb-shaped cholesterol-rich domain at the plasma membrane. Here, we visualized the spatiotemporal interactions between TRPV4 and cholesterol at the plasma membrane in living cells by dual-color single-molecule imaging using total internal reflection fluorescence microscopy. To this aim, we labeled cholesterol at the cytosolic leaflets of the plasma membrane using a cholesterol biosensor, D4H. Our single-molecule tracking analysis showed that the TRPV4 molecules colocalize with D4H-accessible cholesterol molecules mainly in the low fluidity membrane domains in which both molecules are highly clustered. Colocalization of TRPV4 and D4H-accessible cholesterol was observed both inside and outside of caveolae. Agonist-evoked TRPV4 activation remarkably decreased colocalization probability and association rate between TRPV4 and D4H-accessible cholesterol molecules. Interestingly, upon TRPV4 activation, the particle density of D4H-accessible cholesterol molecules was decreased and the D4H-accessible cholesterol molecules in the fast-diffusing state were increased at the plasma membrane. The introduction of skeletal dysplasia-associated R616Q mutation into the CRAC/CARC motif of TRPV4, which reduced the interaction with cholesterol clusters, could not alter the D4H-accessible cholesterol dynamics. Mechanistically, TRPV4-mediated Ca^{2+} influx and the C-terminal calmodulin-binding site of TRPV4 are essential for modulating the plasmalemmal D4H-accessible cholesterol dynamics. We propose that TRPV4 remodels its surrounding plasmalemmal environment by manipulating cholesterol dynamics through Ca^{2+} influx.

SIGNIFICANCE Despite the critical roles of plasmalemmal cholesterol in the formation of nanodomains with other lipids and membrane proteins, the molecular dynamics of cholesterol and membrane proteins at the plasma membrane remain unclear. In this study, we developed a single-molecule live cell imaging of cholesterol by making use of a cholesterol biosensor, D4H. By combination with the imaging of TRPV4, which possesses a cholesterol-interacting motif, we found that cholesterol and TRPV4 interact at the cytosolic leaflets of the plasma membrane. Surprisingly, the TRPV4 activation caused a decrease in particle density and an increase in mobility of plasmalemmal D4H-accessible cholesterol. Our present study suggests a new mode of the regulation of plasmalemmal D4H-accessible cholesterol dynamics by TRPV4-mediated Ca^{2+} influx.

INTRODUCTION

Transient receptor potential vanilloid 4 (TRPV4) is a Ca^{2+}-permeable nonselective cation channel activated by various stimuli (e.g., temperature, osmotic stress, mechanical cues, chemical agonists) (1). Mammalian TRPV4 is ubiquitously expressed in several tissues, including cardiovascular, nervous, and skeletal muscle tissues (1). Pathologically, over 60 mutations have been identified in the human *TRPV4* gene in various skeletal disorders and neuropathies (2). TRPV4 is mainly localized at the plasma membrane as a tetrameric channel (3). Each subunit consists of six transmembrane segments

Submitted August 2, 2023, and accepted for publication February 29, 2024.

*Correspondence: sako@riken.jp or marita@keio.jp

Editor: Sarah Veatch.

https://doi.org/10.1016/j.bpj.2024.02.030

(S1–S6), and the S5–S6 region forms the cation-permeable pore (3). The N- and C-terminal regions face the cytosol and contain a variety of functional domains (e.g., an ankyrin repeat domain at an N-terminus, a calmodulin [CaM]-binding domain at a C-terminus), which are involved in protein-protein interactions (3,4). The activities of TRPV4 are regulated by its surrounding lipid environment (5). For instance, phosphatidylinositol 4,5-bisphosphate ($PI(4,5)P_2$), a phospholipid enriched at the plasma membrane, interacts with TRPV4 and suppresses agonist-evoked TRPV4 activation in HEK293 cells (6). Supplementation of polyunsaturated fatty acids and their metabolites enhance agonist-evoked TRPV4 activation both in *C. elegans* and endothelial cells (7–9). The effects of cholesterol on TRPV4 activation are cell context dependent. Cholesterol positively regulates TRPV4 activation in Muller glia (10), while the opposite effect was observed in human trabecular meshwork cells (11). Caveolae, cholesterol-enriched bulb-shaped invaginations at the plasma membrane, support TRPV4-mediated vasodilation in endothelial cells (12). Thus, the regulation of TRPV4 depends on the proper distribution of membrane lipids at the plasma membrane.

Cholesterol is an essential structural component of cellular membranes in mammalian cells, providing structural integrity for lipid bilayers (13). Cholesterol is enriched at the plasma membrane and recycling endosomes (14,15), accounting for 40%–50% of all plasmalemmal lipids (16–18). Plasma membrane cholesterol interacts with other membrane lipids to generate diverse nanodomains. At the exofacial plasma membrane leaflet, cholesterol interacts with sphingomyelin (SM) and ganglioside GM1 to form nanoscale assemblies called "lipid rafts" (19). At the cytosolic plasma membrane leaflet, cholesterol interacts with phosphatidylserine (PS) to be properly distributed among the plasma membrane leaflets (20). This stabilizes the trans-bilayer coupling of glycosylphosphatidylinositol-anchored proteins and actin filaments (21) and promotes Ras proteins nanoclusters (22). Cholesterol and PS also participate in caveolae formation (23). Caveolae are well-characterized and bulb-shaped membrane domains with a diameter of 60–80 nm, enriched with cholesterol and SM (24). Caveolin-1 (Cav-1) is one of the major components of caveolae and is frequently used as a caveolae marker (24).

Besides plasmalemmal lipids, cholesterol directly interacts with membrane proteins *via* the cholesterol recognition/interaction amino acid consensus (CRAC) motif and its inverted CARC motif on membrane proteins (25,26). TRPV4 possesses the CRAC/CARC motif in its amino acid sequence, located within the S4–S5 helix of each subunit (27), which is evolutionarily conserved among vertebrates (27). It is also a hot spot for numerous point mutations associated with several hereditary bone diseases (2), such as R616Q and V620I mutations identified in patients with autosomal dominant branchyolmia, and the Y602C mutation identified in patients with spondylometaphyseal dysplasia and Kozlowski type (28,29). All the TRPV4 mutants exert a gain-of-function effect, enhancing the basal activity and agonist responsiveness (28,30). Since $TRPV4^{R616Q}$ loses the potency to interact with cholesterol *in vitro* and colocalize with Cav-1 in osteogenic Saos2 cells and in dorsal root ganglion neuron-derived F11 cells (31), loss of cholesterol interaction could be correlated with the gain-of-function effect of TRPV4. As the CRAC/CARC motifs in TRPV4 are located spanning into the cytosolic leaflets of the plasma membrane, TRPV4 can directly interact with cholesterol at the plasma membrane of living cells.

In this study, we established a dual-color single-molecule imaging system for TRPV4 and cholesterol using total internal reflection fluorescence microscopy. Using a D434S mutant of the cholesterol-binding D4 domain (called D4H) derived from perfringolysin O (PFO) as a cholesterol visualizing probe (32), we scrutinized the spatiotemporal colocalization between TRPV4 and D4H at the plasma membrane of living HeLa cells. Notably, agonist-evoked Ca^{2+} influx via TRPV4 decreased D4H-accessible cholesterol molecules at the cytosolic plasma membrane leaflets. This TRPV4-mediated cholesterol reduction was accompanied by a decrease in the less mobile cholesterol nanoclusters and an increase in the highly mobile cholesterol. Mutations in the cholesterol and CaM-binding sites attenuated the changes in cholesterol dynamics by TRPV4-mediated Ca^{2+} influx. Our findings suggest a novel mechanism of cholesterol homeostasis at the plasma membrane, controlled by TRPV4-mediated Ca^{2+} influx.

MATERIALS AND METHODS

Construction of cDNA

The human TRPV4-coding sequences (cloned from the MegaMan Human Transcriptome Library) were amplified with PCR and inserted into the pFN21A HaloTag cytomegalovirus Flexi Vector (Promega) to fuse the HaloTag to the N-terminus of the expressed protein as previously described (33). TRPV4 without HaloTag was generated by PCR using primers to exclude the HaloTag coding sequence. Three human TRPV4 mutants (R616Q, Δ812-831, and W822A) were generated by PCR using the primer containing mutated sequences. The pEGFP-N1 (CMVd1) vector was constructed by inserting an IRES-Neo sequence and partially deleting cytomegalovirus promotor in pEGFP-N1 vector (Clontech). To construct the N-terminally SNAP-tagged D4H, the SNAP-tag (New England Biolabs) and the D4H coding sequence were amplified by PCR and exchanging the EGFP sequence into the pEGFP-N1 (CMVd1) vector. For triple-color single-molecule imaging using EGFP-Cav-1, the human Cav-1 was N-terminally fused to EGFP using the pEGFP-C3 vector (Clontech) as a backbone.

Cell culture

HeLa cells were maintained in DMEM supplemented with 10% fetal bovine serum (FBS) (HyClone, Cat: SH30088.03) at 37°C under 5% CO_2. Transfection was performed by using a Lipofectamine 3000 Transfection Reagent. A transfection solution was mixed by combining plasmid plus

P3000 reagent a solution diluted in Opti-MEM and Lipofectamine 3000 reagent in Opti-MEM, according to the manufacturer's instructions. The amounts of plasmids were described per experiment below. For the generation of a HeLa cell line stably expressing SNAP-tagged D4H (HeLa/SNAP-D4H), HeLa cells were transfected with the vector containing SNAP-D4H. At 24 h after transfection, the cells were selected with fresh 10% FBS/DMEM containing 1 mg/mL Geneticin (Thermo Fisher Scientific, Cat: 10,131-035) for 3 weeks, and the stable cell line was cloned. For cholesterol depletion or supplementation, HeLa cells were incubated with 0–10 mM MβCD (Wako; Cat: 320–84252) or 0–1 mM cholesterol/MβCD complexes (Sigma-Aldrich; Cat: C4951) diluted in DMEM for 1 h at 37°C. To chelate extracellular Ca^{2+}, HeLa cells were incubated in HBSS supplemented with 20 mM EGTA (Wako; Cat: 342–01314) before experiments.

Single-molecule imaging

For dual-color single-molecule imaging of D4H and TRPV4, plasmid DNAs (0.1 μg per 60-mm dish) encoding HaloTag-fused TRPV4 (wild type [WT] and its mutants) were transfected into HeLa/SNAP-D4H cells on glass coverslips (Matsunami) in a 60-mm dish 1 day before imaging. In the case of triple-color single-molecule imaging, plasmid DNAs (0.2 μg per 60-mm dish) encoding EGFP-Cav-1 were cotransfected with HaloTag-fused TRPV4. After overnight incubation, the SNAP-tag and HaloTag were labeled for 15 min at 37°C with 10 nM SNAP-Cell TMR-Star ligand (New England Biolabs; Cat: S9105S) and 30 nM SF650 HaloTag ligand (Goryo Chemical, Cat: A308-02), respectively, in DMEM without phenol red. After washing with 3 mL 10% FBS/DMEM three times, the cells incubated for 1 h at 37°C. Mounting the cells on a coverslip on the Attofluor Cell Chamber (Thermo Fisher Scientific; Cat: A7816), washing with 400 μL 0.01% BSA/Hank's balanced salt solution (HBSS) (Sigma-Aldrich; Cat: H1387-10X1L) three times.

Single-molecule imaging was performed by a homemade quad-color TIRF microscope system with a 488-nm, 30-mW laser (OBIS 488, Coherent) for EGFP, with a 561 nm, 50 mW-laser (OBIS 561, Coherent) TMR, and with a 637-nm, 100 mW laser (OBIS 637, Coherent) for SF650 through the objective (PlanApo 100×, NA 1.49, Nikon) by a dichroic mirror (ZT405/488/561/640, Chroma). Fluorescence images were spectrally split into four channels using image splitting optics with two W-view Gemini (Hamamatsu; Cat: A12801-01) connected in tandem to a W-view Gemini-2C (Hamamatsu; Cat: A12801-10) and captured simultaneously by two sCMOS cameras (ORCA Fusion BT; Hamamatsu; Cat: C15440-20UP). In the image splitting optics, dichroic mirrors (FF640-FDi01, Semrock, in W-view Gemini-2C, T720lpxr-UF1, Chroma, in a W-view Gemini for long wavelength, and T560lpxr-UF21, Chroma for short wavelength) and emission filters (ET685/50m, Chroma for SF650, FF01-600/52-25, Semrock for TMR, and ET525/50m, Chroma for EGFP) were included to split images (512 × 512 pixels images, pixel size: 65 nm/pixel). The TIRF microscope system was controlled by AIS, Zido (https://eng.zido.co.jp/). We took 100 frame movies per cell with a 30.5-ms exposure time before and from 1 to 5 min after 100 μL vehicle solution or ligand (GSK101; Cayman, Cat: 17289 and ionomycin, Sigma-Aldrich, Cat: I3909, solution at five times the final concentration) addition. The final concentration of GSK101 and ionomycin was of 300 nM and 1 μM, respectively.

Single-molecule tracking analysis

The multiple TIFF files (16-bit) processing (subtract background with 25 pixels rolling ball radius) were performed by ImageJ with batch processing macro (https://github.com/masataka-yanagawa/ImageJ-macro-ImageProcessingSMT). The alignment between the two channels based on the images of multi-color beads (TetraSpeck Microspheres; Thermo Fisher Scientific; Cat: T7279) was performed using AAS, Zido (https://eng.zido.co.jp/). The single-molecule tracking analysis and variational Bayesian-hidden Markov model was performed using AAS with the following parameters: detection mode, Gauss fit scanning; region of interest, 12 pixels; interval, 3 pixels; intensity threshold, 25 arbitrary units; maximum connection frame, 2 frames; maximum connection length, eight pixels; minimum trajectories frame, 12 frames; connection mode, nearest neighbor; analysis mode, SimpleVbSPT; and estimation mode, maximum probability. According to above parameters, only the brighter spot is detected when the center coordinates of adjacent spots are within 3 pixels (195 nm). Two spots are connected as a trajectory of a single molecule when detected in successive frames within 8 pixels (520 nm) and within the two frames. Given that hidden Markov model analysis requires trajectory lengths of at least 12 frames, the analysis does not include information from shorter trajectories. When the trajectory length constraint is removed (detection of at least 1 frame), nearly all visually confirmable spots are detected. Under the trajectory length constraint of at least 12 frames, more than 70% of those spots were detected in our single-molecule tracking analysis (Fig. S2 *A*). All subsequent analyses (trajectory, density, diffusion dynamics, intensity distribution, colocalization, and statistical analysis) were performed using smDynamicsAnalyzer (https://github.com/masataka-yanagawa/IgorPro8-smDynamicsAnalyzer), an Igor Pro-based homemade program.

The colocalization of two particles is detected if the two particles are within 100 nm in the same frame and are in the same diffusion state as previously described (34). The positional accuracy of each localization was estimated based on the formula: $Variance(\mu_x) = \frac{\sigma_a^2}{N}\left(\frac{16}{9}+\frac{8\pi\sigma_a^2 ab^2}{Na^2}\right)$ (35), where N is the number of photons in the image, σ is the SD of a two-dimensional Gaussian function, a is pixel size (67 nm/pix in this study), and b^2 is background noise. As a result, the position accuracy of both SF650-labeled TRPV4 and TMR-labeled D4H molecules is approximately 6 nm (Fig. S2 *B* and *C*). When the alignment error between channels (17 nm) calculated from the fluorescent beads is considered, the total positional accuracy is approximately 20 nm in SD. The threshold value of 100 nm used in the current colocalization analysis corresponds with 5 SD, which is high enough to avoid false-negative determinations. The diffusion coefficients of each diffusion state of TRPV4 and D4H are as follows: TRPV4: immobile, 0.008 $\mu m^2/s$; medium, 0.030 $\mu m^2/s$; and fast, 0.20 $\mu m^2/s$. D4H: immobile, 0.010 $\mu m^2/s$; medium, 0.050 $\mu m^2/s$; and fast, 0.30 $\mu m^2/s$. Also, the displacement histograms in each state were overlapped (Fig. S3 *C* and *D*). Therefore, it would be appropriate to use the same diffusion states as a criterion in the colocalization analysis. The probability of colocalization and the apparent binding affinity (K_B) between molecules A and B in the cell of membrane area S were calculated as follows;

$$P_{col} = \frac{[A\cdot B]}{[A]tot} \text{ or } P_{col} = \frac{[A\cdot B]}{[B]tot}, K_B = \frac{[A\cdot B]}{[A][B]},$$

where $[A \cdot B]$ = (the number of the colocalized steps per frame)/S, $[A]_{tot}$ = (the total step number of A per frame)/S, $[B]_{tot}$ = (the total step number of *B* per frame)/S, $[A] = [A]_{tot} - [A \cdot B]$, and $[B] = [B]_{tot} - [A \cdot B]$. The membrane area *S* was estimated from the density analysis as follow. The density was estimated as the plateau value of the mean local density function as described previously (36). Then, the membrane area *S* was estimated as the "number of spots/density" (36). Normalized density was calculated as the density from 1 to 5 min after stimulation divided by the density before stimulation of the same cell. Changes in the fractions in the diffusion states and density histograms were the differences before and from 1 to 5 min after stimulation of the same cell. The on-event rate was calculated as the initial slope of the cumulative event number divided by *S* (36).

To estimate the random colocalization, the two colocalization analyses using the data acquired from pixel shifting and simulations were performed. In the pixel shifting analysis, the new trajectories were created by shifting the original trajectories of Halo-tagged TRPV4 (Halo-TRPV4) or Halo-CD86 horizontally by 2–16 pixels (130–1040 nm) (37,38). The colocalization analysis was then performed under the same criteria described above using the shifted Halo-TRPV4 and Halo-CD86 trajectories, and the original

SNAP-D4H trajectories. In the simulation, a series of simulated data were generated as follows. First, the initial x and y coordinates of a given number of molecules (250, 500, 750, and 1,000) were randomly distributed in a square space of (P, P) − (512–P, 512–P). Here, P is the pixel size that provides a buffer area to avoid trajectories extending outside the image (10 pixels for the colocalization analysis). Second, the initial diffusion state of each molecule was determined in accordance with the experimentally estimated initial fraction of each diffusion state by means of a uniform random number. Third, the diffusion state of each molecule in the second and subsequent frames was generated by a time evolution based on the state of the previous frame and the experimentally estimated transition probabilities between diffusion states. In the time evolution step, the displacements in the X and Y directions were determined by multiplying $\sqrt{2D\Delta t}$ by a normal random number with a mean of 0 and SD of 1, respectively. The values of parameters (initial fraction of the diffusion state, transition probability, diffusion coefficient) were determined from the dual-color single-molecule imaging of Halo-TRPV4/SNAP-D4H or Halo-CD86/SNAP-D4H. The diffusion coefficient values of each diffusion state of TRPV4 and D4H were as follows; TRPV4 (immobile, 0.008 $\mu m^2/s$; medium, 0.030 $\mu m^2/s$; and fast, 0.20 $\mu m^2/s$) and D4H (immobile, 0.010 $\mu m^2/s$; medium, 0.050 $\mu m^2/s$; and fast, 0.30 $\mu m^2/s$). The diffusion coefficient values of each diffusion state of CD86 and D4H were as follows: CD86 (immobile, 0.010 $\mu m^2/s$; medium, 0.040 $\mu m^2/s$; and fast, 0.25 $\mu m^2/s$) and D4H (immobile, 0.010 $\mu m^2/s$; medium, 0.040 $\mu m^2/s$; and fast, 0.30 $\mu m^2/s$). The colocalization analysis using the simulated data was then performed under the same criteria described above. The density analysis described above using the simulated data confirmed that the estimated density was almost identical to the theoretical density (Fig. S2 *J* and *K*). The theoretical membrane area was defined as the area in the range of (P, P) − (512–P, 512–P). Regardless of the density, the membrane area S estimated by the algorithm described above was approximately the same as the theoretical area (Fig. S2 *L* and *M*; dashed black lines).

Confocal imaging

For the quantification of TRPV4 localization, plasmid DNAs (0.5 μg per 60-mm dish) encoding HaloTag-fused $TRPV4^{WT}$ were transfected into HeLa cells on glass coverslips (Matsunami) in a 60-mm dish 1 day before imaging. After overnight incubation, the HaloTag were labeled for 15 min at 37°C with 100 nM Janelia Fluor 549 HaloTag Ligand (JF549, Promega; Cat: GA1110) in DMEM without phenol red. After washing with 3 mL 10% FBS/DMEM three times, the cells were incubated for 1 h at 37°C. For labeling of the plasma membrane, the cells were treated with CellMask Deep Red Plasma Membrane Stains (CellMask, 1:10,000 dilution in BSA/HBSS, Thermo Fisher Scientific; Cat: C10046) for 3 min at room temperature. After washing with 3 mL BSA/HBSS three times, the cells on a coverslip were mounted on the Attofluor Cell Chamber (Thermo Fisher Scientific).

For the visualization of PS exposure by using Annexin V-FITC Early Apoptosis Detection Kit (Cell Signaling Technology; Cat: 6592), plasmid DNAs (0.2 μg per well in a 12-well plate) encoding HaloTag-fused $TRPV4^{WT\ or\ R616Q}$ were transfected into HeLa cells on the glass coverslips 1 day before experiment. After overnight incubation, the HaloTag was labeled for 15 min at 37°C with 100 nM SF650 HaloTag ligand in DMEM without phenol red. After washing with 500 μL DMEM twice, the cells on a coverslip were mounted on a Chamlid imaging chamber (Chamlide CMB; Cat: CM-B15-1). After adding 400 μL 1× Annexin V Binding Buffer supplemented with Annexin V-FITC, the cells were incubated for 10 min at room temperature in the dark.

Confocal images were then obtained using an FLUOVIEW FV3000 confocal upright microscope and operated with FLUOVIEW FV31S-SW software (Olympus). The FV3000 microscope was equipped with a water-immersion×40 (LUMPlanFL N, 0.80 NA, Olympus). Excitation wavelengths of lasers applied for the FV3000 microscope were 488 nm for Annexin V-FITC, 561 nm for JF549, and 640 nm for CellMask, respectively. Fluorescence images were acquired sequentially to avoid cross-detection of the fluorescent signals. To quantify the localization of TRPV4 to the plasma membrane using ImageJ, the fractions of the plasma membrane were extracted from JF549 images utilizing the CellMask images. Cells that were saturated with the JF549 signal were excluded from the analysis.

Western blotting

Plasmid DNAs (0.5 μg per 60-mm dish) encoding $TRPV4^{WT}$ were transfected into HeLa cells in a 60-mm dish 1 day before experiments. After overnight incubation, the cells were collected by centrifugation, and the pellet was washed with 1 mL PBS three times. The cell pellets were resuspended in a lysis buffer (1% *n*-dodecyl-β-D-maltoside; 50 mM HEPES, 140 mM NaCl, pH 6.5). After centrifugation at 15,000 rpm for 10 min, the lysates were stored at −30°C. The lysates were suspended with sample buffer (50 mM Tris-HCl [pH 6.8], 1% SDS, 5% glycerol, 0.5 M β-mercaptoethanol, 1 mM EDTA). After being separated by 10% SDS-PAGE, the electrophoresed proteins were transferred onto a polyvinylidene difluoride membrane. The blotted membrane was blocked with 5% skim milk-containing blotting buffer (10 mM Tris-HCl [pH 7.4], 70 mM NaCl, and 0.05% Tween 20) and immunoblotted with primary and secondary antibodies. Primary antibodies used in this study were anti-TRPV4 rabbit polyclonal antibody (1:1,000 dilution, Alomone Labs; Cat: ACC-034), anti-SNAP-tag rabbit polyclonal antibody (1:1,000 dilution, GenScript; Cat: A00684-40) and anti-β-actin (1:10,000 dilution, Sigma-Aldrich; Cat: A5441). Secondary antibodies were horseradish peroxidase-linked anti-rabbit immunoglobulin G (1:2,000 dilution, Cell Signaling Technology; Cat: 7074S) and anti-mouse immunoglobulin G (1:10,000 dilution, Cell Signaling Technology; Cat: 7076S). Immunoreactive proteins were detected with Amersham ECL Prime Western Blotting Detection Reagent (GE Healthcare) using ImageQuant LAS 500 (GE Healthcare). The density of bands was quantified by ImageJ.

FLIPR calcium mobilization assay

Plasmid DNAs (1.0 μg per 96-well plate) encoding HaloTag-fused TRPV4 (WT and its mutants) were transfected into HeLa cells in a Collagen I 96-well Black/Clear Plate (BioCoat, Corning; Cat: 354649) 1 day before the experiment. After overnight incubation, the cells were incubated for 1.5 h with the calcium indicator (FLIPR Calcium 6 Assay Kit; Cat: R8191) in 80 μL BSA/HBSS at 37°C under 5% CO_2 and then for 30 min at room temperature. Calcium influx was detected with a microplate reader (FlexStation3; Molecular Devices) with the following parameters: mode, fluorescence; excitation, 485 nm; shut-down, 515 nm; emission, 525 nm; photomultiplier gain, automatic; flashes per reading, 6; and read from the bottom. Ligand (20 μL GSK101 and ionomycin solution at 5 times the final concentration) was added 30 s after the start of measurements. The final concentration of GSK101 and ionomycin was of 300 nM and 1 μM, respectively. The calcium influx trace and the dose-response curves were analyzed using the peak fluorescence intensity normalized to the fluorescence intensity of vehicle treatment control. The dose-response curves were fitted with the Hill Equation (Eq. 1) with Igor Pro 9.0.

$$f(x) = \mathit{minimal\ response} + \frac{\mathit{maximal\ response} - \mathit{minimal\ response}}{1 + \left(\frac{EC_{50}}{x}\right)^{n}}, \quad (1)$$

where n is the Hill coefficient.

Saturation binding assays of TMR and SF650

For saturation binding assay of TMR, parental HeLa cells or HeLa/SNAP-D4H cells were seeded in a Collagen I 96-well Black/Clear Plate (BioCoat,

Corning; Cat: 354649) 1 day before the experiment. For saturation binding assay of SF650, plasmid DNAs (1.0 μg per 96-well plate) encoding untagged TRPV4^{WT} or HaloTag-fused TRPV4^{WT} were transfected into HeLa/SNAP-D4H cells in a Collagen I 96-well Black/Clear Plate 1 day before the experiment. After overnight incubation, the SNAP-tag and HaloTag were labeled for 15 min at 37°C with 0–3 μM SNAP-Cell TMR-Star ligand and 0–1 μM SF650 HaloTag ligand, respectively, in DMEM without phenol red. After washing with 10% FBS/DMEM three times, the cells were incubated for 1 h at 37°C. The saturation binding of the HaloTag ligand was detected with a microplate reader (Tecan SPARK Plate Reader, Tecan) with the following parameters: mode, fluorescence; excitation, 530 nm; emission, 585 nm for TMR; and excitation, 635 nm; emission, 680 nm for SF650; gain, 100; flashes per read, 30; and read from top. The background fluorescence intensity was estimated from the intensity of cells untreated with the TMR or SF650. The total binding of TMR and SF650 was determined from the fluorescence intensity of HeLa/SNAP-D4H cells and HaloTag-fused TRPV4^{WT}-transfected HeLa cells, respectively. Nonspecific binding of TMR and SF650 was determined from the fluorescence intensity of parental HeLa cells and untagged TRPV4^{WT}-transfected HeLa cells, respectively. Specific binding was calculated as the difference between the total binding and nonspecific binding. The data were fitted with the Hill Equation (Eq. (1)).

As shown in Fig. S3 *L*, higher nonspecific binding was observed at SNAP-TMR concentrations above 100 nM. Although the coverslips were thoroughly washed for single-molecule imaging after labeling, similar washing was difficult in 96-well plates because of cell detachment. During TIRF measurements, few bright spots were observed around the cells on the coverslips after the extensive washing procedure (Fig. 1 *B*, *D*, and *F*).

Statistical analysis

Statistical analyses were performed using Igor Pro 9 software and methods are described in the legends of the figures. Representation of symbols and error bars is described in the legends. Symbols are either mean values of indicated numbers of independent experiments or numbers of measured cells from a single experiment. The error bars and shaded areas denote the SEM. Statistical significance was determined using one-way ANOVA followed by Dunnett's test or Tukey HSD test, two-tailed Student's *t*-test.

RESULTS

Cholesterol suppresses TRPV4-mediated Ca^{2+} influx in HeLa cells

As the effects of cholesterol on TRPV4 activation are cell-context dependent (10,11), we performed a calcium mobilization assay using TRPV4-expressing HeLa cells after depleting or supplementing cholesterol. Fig. S1 *A* and *B* show that treating TRPV4-expressing HeLa cells with methyl-beta-cycloheximide (MβCD) enhanced the GSK101 (GSK1016790A; a TRPV4 agonist)-evoked Ca^{2+} influx in an MβCD dose-dependent manner. Cholesterol depletion significantly increased the maximal response of Ca^{2+} influx (Fig. S1 *C*). Supplementing cholesterol by treating the TRPV4-expressing HeLa cells with a cholesterol/MβCD complex suppressed GSK101-evoked Ca^{2+} influx and significantly decreased the maximal response in a cholesterol/MβCD complex dose-dependent manner (Fig. S1 *D–F*). Both the protein expression level and plasmalemmal localization of expressed TRPV4 were unaffected by the depletion or supplementation of cholesterol in HeLa cells (Fig. S1 *G–L*), suggesting that cholesterol suppresses GSK101-mediated TRPV4 activation in HeLa cells.

Spatiotemporal interactions between TRPV4 and cholesterol visualized by a dual-color single-molecule imaging

We analyzed the TRPV4/cholesterol interaction at the plasma membrane of live HeLa cells. To achieve this, we generated a stable HeLa cell line expressing SNAP-tagged D4H (SNAP-D4H), a biosensor for cholesterol at the cytosolic plasma membrane leaflet (Fig. 1 *A*) (20). As a control, we coexpressed the EGFP-PLCδ-PH domain, a binding probe for $PI(4,5)P_2$ enriched in the cytosolic plasma membrane leaflets. Then, we simultaneously visualized D4H and PLCδ-PH via total internal reflection fluorescence microscopy (Fig. 1 *B*). MβCD treatment of the cells reduced the D4H signals in the evanescent field but did not affect the PLCδ-PH signal, indicating that D4H-accessible cholesterol was removed from the cytosolic plasma membrane leaflets (Fig. 1 *B* and *C*). These results indicate that our total internal reflection fluorescence microscopy system, with SNAP-D4H expressing cells, can successfully visualize D4H-accessible cholesterol in the cytosolic plasma membrane leaflets of living cells.

Next, we expressed Halo-TRPV4 (33) in SNAP-D4H stably expressing HeLa cells and simultaneously stained with SNAP-TMR and Halo-SF650 ligands. Then, we analyzed the colocalization between TMR-labeled D4H and SF650-labeled TRPV4 at a single-molecule resolution (Fig. 1 *A*). We observed that D4H and TRPV4 colocalized at the plasma membrane in living cells with and without GSK101, a selective TRPV4 agonist (Fig. 1 *D–F* and Videos S1 and S2). After single-molecule tracking analysis (Fig. S2 *A*), we performed a colocalization analysis based on two criteria. Two particles are defined to be colocalized (1) if the two particles are localized within 100 nm in the same frame, which corresponds with 5 SD of the total position accuracy (Fig. S2 *B* and *C*), which is high enough to avoid false-negative determinations, and (2) if the two particles exhibit the same diffusion state. We estimated the random colocalization probability by dual-color single-molecule imaging with D4H using CD86, which does not possess cholesterol-interacting motifs, to be approximately 0.4% (Fig. 1 *G*; a black dashed line). The colocalization probability between D4H and TRPV4 (approximately 1.2%) was higher than the random colocalization (Fig. 1 *G*). GSK101 stimulation significantly decreased the colocalization between TRPV4 and D4H molecules compared with the control (Fig. 1 *G*). To compensate for the difference in the density, we calculated an apparent K_B, which represents the density of the colocalized particles normalized to the product of the densities of free TRPV4 and D4H particles (Fig. 1 *H*) (see Methods). Similarly, we calculated the K_B between CD86 and D4H as a null control (Fig. 1 *H*; black dashed line). Even with the

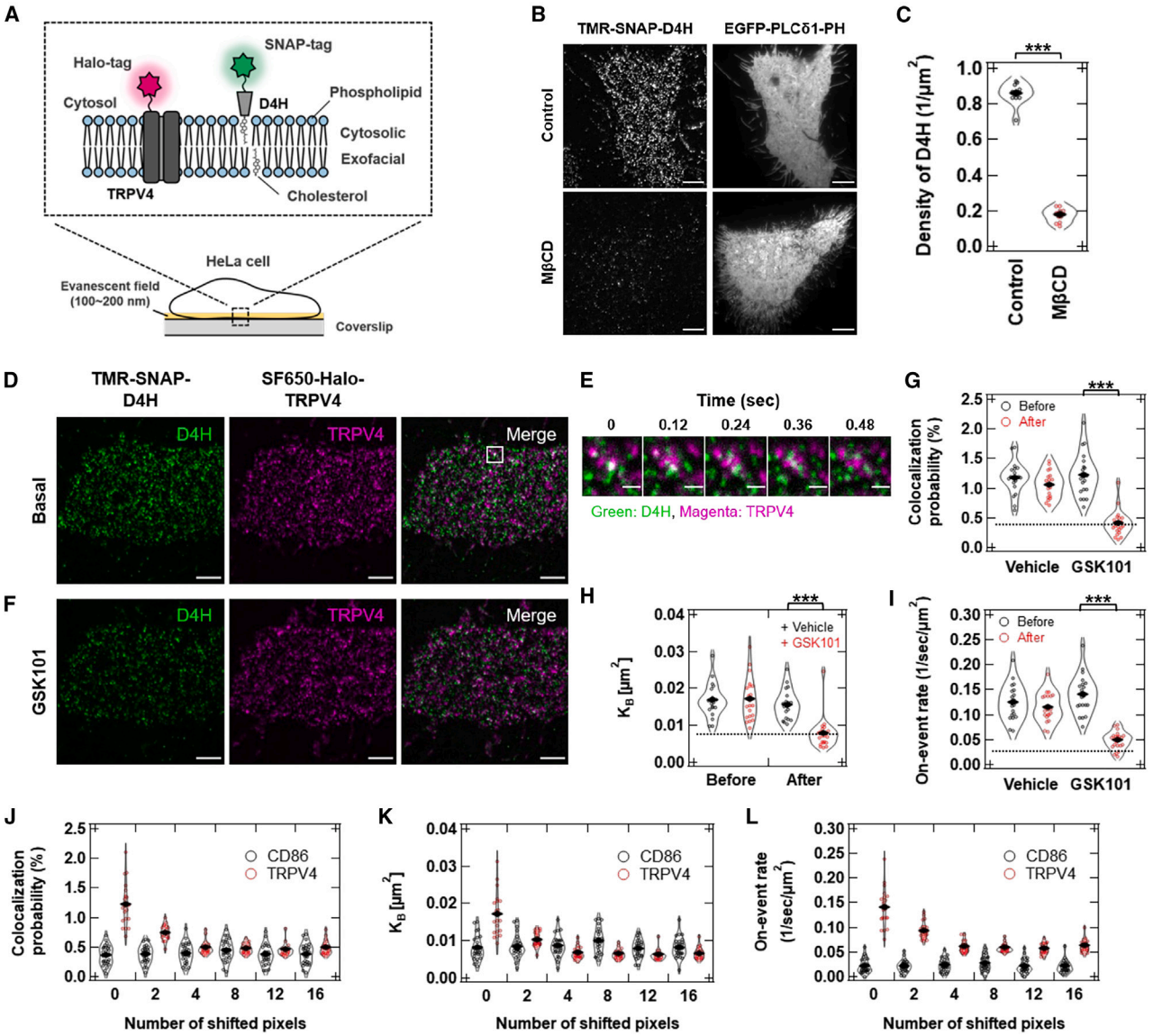

FIGURE 1 Spatiotemporal interactions between D4H-accessible cholesterol and TRPV4 upon TRPV4 activation. (*A*) A scheme of the dual-color single-molecule imaging of SNAP-D4H and Halo-TRPV4 by a total internal reflection fluorescence microscopy (TIRFM). (*B*) Representative TIRFM images of TMR-labeled D4H in HeLa cells expressing EGFP-PLCδ-PH. EGFP-PLCδ-PH was used as a marker of the plasma membrane. Scale bars, 5 μm. (*C*) The density of D4H shown in (*B*) was quantified. Violin plots show the mean value and distribution of 10 cells (two-tailed *t*-test). ***$p < 0.001$ (two-tailed *t*-test). (*D*) Representative TIRFM images of TMR-labeled D4H (green) and SF650-labeled TRPV4 (magenta) at the basal state before stimulation. Scale bars, 5 μm. Magnified sequential images of a white square during live cell imaging were shown in (*E*). (*E*) Representative images of the colocalization of TMR-labeled D4H (green) and SF650-labeled TRPV4 (magenta) in living cells. Scale bars, 1 μm. (*F*) Representative TIRFM images of TMR-labeled D4H (green) and SF650-labeled TRPV4 (magenta) 5 min after stimulation with 300 nM GSK1016790A (GSK101). Scale bar; 5 μm. (*G*) Colocalization probability of TRPV4 with D4H before and from 1 to 5 min after stimulation with the indicated condition (vehicle, 300 nM GSK101). The percentages represent the proportion of TRPV4 molecules colocalized with D4H to the total number of TRPV4 molecules. Violin plots show the mean value and distribution of 20–22 cells. ***$p < 0.001$ (two-tailed *t*-test). A dashed black line represents the false-positive threshold estimated from the mean value for the random colocalization condition between SF650-labeled CD86 and TMR-labeled D4H (see also Fig. 1 *J*; the black circle when number of shifted pixels is 0). (*H*) TRPV4-D4H K_B before and from 1 to 5 min after GSK101 stimulation with the indicated condition (vehicle, 300 nM GSK101). Violin plots show the mean value and distribution of 20–22 cells. ***$p < 0.001$ (two-tailed *t*-test). A dashed black line represents the false-positive threshold of the K_B calculated from the mean value for the random colocalization condition between SF650-labeled CD86 and TMR-labeled D4H (see also Fig. 1 *K*; the black circle when number of shifted pixels is 0). (*I*) TRPV4-D4H association (on-event) rates calculated from all trajectories before and from 1 to 5 min after stimulation with the indicated condition (vehicle, 300 nM GSK101). Violin plots show the mean value and distribution of 20–22 cells. ***$p < 0.001$ (two-tailed *t*-test). A dashed black line represents the false-positive threshold of the on-event rate calculated from the mean value for the random colocalization condition between SF650-labeled CD86 and TMR-labeled D4H (see also Fig. 1 *L*; the black circle when number of shifted pixels is 0). (*J–L*) The colocalization probability (*J*), K_B (*K*), and on-event rate (*L*) of CD86 with D4H (black circles) and TRPV4 with D4H (red circles) obtained from colocalization analysis of SNAP-D4H with Halo-CD86 or Halo-TRPV4 shifted horizontally by 2–16 pixels (130–1040 nm). The data when number of shifted pixels is 0 represents the original pre-processed data. Violin plots show the mean value and distribution of 22–26 cells.

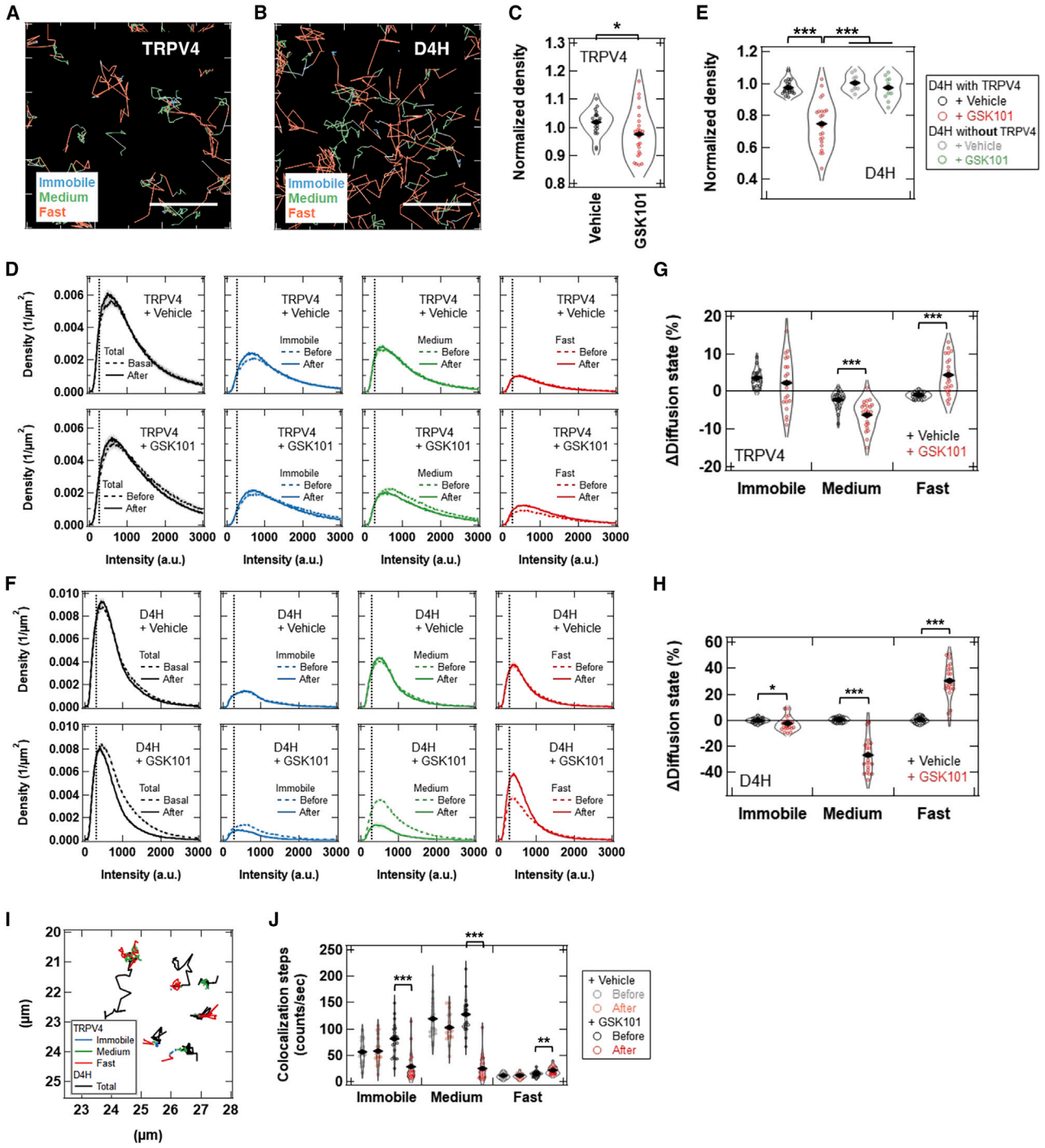

FIGURE 2 TRPV4 activation alters the dynamics of D4H-accessible cholesterol at the plasma membrane. (*A*, *B*) Each step in the trajectories of TRPV4 (A) and D4H (*B*) molecules at the plasma membrane was categorized into three diffusion states. The immobile, medium, and fast states were shown in blue, green, and red, respectively. Scale bars, 1 μm. (*C–F*) Normalized density and histograms of density acquired by a dual-color single-molecule imaging of TRPV4 and D4H. Density of TRPV4 (*C*) and D4H (*E*) from 1 to 5 min after stimulation with the indicated condition (vehicle, 300 nM GSK101) normalized to the basal state before stimulation of the same cell was calculated from Fig. S3 *M* and *N*. In Fig. 2 *E*, data were obtained from TRPV4-transfected cells ("D4H with TRPV4") and TRPV4-untransfected cells ("D4H without TRPV4"). Violin plots show the mean value and distribution of 20–22 cells. ***$p < 0.001$; *$p < 0.05$ (two-tailed *t*-test). Histograms of density in TRPV4 (*D*) and D4H (*F*) before and from 1 to 5 min after stimulation with the indicated condition (vehicle, 300 nM GSK101) were shown. Dashed black lines represent the intensity of single molecules estimated from SF650-labeled CD86 (210 arbitrary units [a.u.]) and TMR-labeled CD86 (280 a.u.) (the monomeric control; see also Fig. S3 *G* and *H*). (*G*, *H*) Changes in the fractions in the diffusion states of TRPV4 (*G*) and D4H (*H*) molecules before and from 1 to 5 min after stimulation with the indicated condition (vehicle, 300 nM GSK101) were calculated from Fig. S3 *O* and *P*. Violin plots show the mean value and distribution of 20–22 cells. ***$p < 0.001$; *$p < 0.05$ (two-tailed *t*-test). (*I*)

(legend continued on next page)

normalization, the K_B between TRPV4 and D4H was higher values than the null case (Fig. 1 *H*). TRPV4 activation significantly decreased the K_B value and association between both molecules (Fig. 1 *H* and *I*).

We also calculated the random colocalization by performing colocalization analysis of D4H with CD86 or TRPV4 shifted horizontally by 2–16 pixels (130–1,040 nm) (37,38). The colocalization probabilities between CD86 and D4H were constant (approximately 0.4%) by shifting pixels (Fig. 1 *J*; black circles). As the pixels were shifted, the colocalization probabilities between TRPV4 and D4H converged to approximately 0.5% (Fig. 1 *J*; red circles). These results suggest that the random colocalization probability was 0.4%–0.5%. The K_B value and on-event rate between CD86 and D4H were constant (approximately 0.008 [μm^2] and 0.025 [1/s/μm^2], respectively) by pixel shifting (Fig. 1 *K* and *L*; black circles). As the pixels were shifted, the K_B value and on-event rate between TRPV4 and D4H converged to approximately 0.008 (μm^2) and 0.06 (1/s/μm^2), respectively (Fig. 1 *K* and *L*; red circles). Additionally, we estimated the random colocalization from a series of simulated data (Fig. S2 *D–F*). The colocalization probabilities and on-event rate between TRPV4 and D4H or CD86 and D4H increased as the particle density increased (Fig. S2 *D* and *F*). The K_B values were constant regardless of the increase in the particle density (Fig. S2 *E*). We found that, at a particle density of 0.70 (μm^{-2}), which corresponds with the experimental conditions (Fig. S3 *M* and *N*), the false detection threshold of the colocalization probability, K_B and on-event rate were approximately 0.5%, 0.008 (μm^2), and 0.05 (1/s/μm^2), respectively (Fig. S2 *D–F*). These results were consistent with the pixel shifting analysis (Fig. 1 *J–L*).

The mean on-time, the duration time in which colocalized spots of TRPV4 and D4H persist together, was not changed by the GSK101 stimulation (Fig. S2 *G*). The values of the mean on-time of TRPV4 with D4H were constant by shifting pixels or by increasing the density, and almost identical to that of CD86 with D4H (Fig. S2 *H* and *I*). These data suggested that the mean on-time of TRPV4 with D4H could not be distinguished from the random associations. Considering the significant decrease in the on-event rate (Fig. 1 *I*), these results suggest that the decrease in the K_B between TRPV4 and D4H upon TRPV4 activation is mainly due to the decrease in the association rate rather than an increase in the dissociation rate (Fig. 1 *H*).

The diffusion coefficient values of each diffusion state of CD86 and TRPV4 were as follows: CD86 (immobile, 0.010 μm^2/s; medium, 0.040 μm^2/s; and fast, 0.25 μm^2/s) and TRPV4 (immobile, 0.008 μm^2/s; medium, 0.030 μm^2/s; and fast, 0.20 μm^2/s). Although the diffusion dynamics were different between CD86 and TRPV4, their false-positive rates of the K_B value measured by pixel-shifting or simulation was almost identical (Fig. 1 *K*). In the simulation, the faster diffusing CD86 tended to exhibit higher false-positive values in the colocalization rate, K_B and on-rate compared with TRPV4 (Fig. S2 *D–F*). In addition, while both colocalization and on-rates between TRPV4 and D4H were affected by changes in density (Fig. S2 *D* and *F*), the K_B values between TRPV4 and D4H were not dependent on the particle density (Fig. S2 *E*). These control experiments suggest that the GSK101-induced decrease in the K_B value between TRPV4 and D4H in Fig. 1 *H* is not due to a decrease in false positive rate associated with changes in particle density or diffusion coefficient upon TRPV4 activation, as described below.

Characterization of the single-molecule diffusion behavior of TRPV4 and D4H at the plasma membrane

To classify the diffusion states of TRPV4 and D4H at the plasma membrane, we performed variational Bayesian-hidden Markov model clustering analyses (36,39). Among the one-to five-state models, the three-state model (immobile, medium, and fast, in ascending order of diffusion coefficients) exhibited the highest likelihood for both TRPV4 and D4H trajectories (Fig. S3 *A* and *B*). We exemplified the trajectories and step-size histograms of TRPV4 and D4H in each state (Figs. 2 *A*, *B*, S3 *C* and *D*). The down-shaped mean square displacement-Δt plots demonstrated that the TRPV4 and D4H molecules in the immobile state exhibited confined diffusion on average (Fig. S3 *E* and *F*) with confinement lengths of 80–150 nm and 60–200 nm, respectively (Fig. S3 *E* and *F*). Contrastingly, the linear mean square displacement-Δt plots indicated that the TRPV4 and D4H molecules in the medium and fast states exhibited simple diffusion (Fig. S3 *E* and *F*).

We examined the oligomeric states of TRPV4 and D4H by analyzing the intensity histograms in each diffusion state. The peak fluorescence intensity of the single molecules was estimated to be 210 arbitrary units for SF650 and 280 arbitrary units for TMR according to the fluorescence intensity histogram for Halo or SNAP-tagged CD86, a monomeric membrane protein (40), respectively (Fig. S3 *G* and *H*). Considering the peak value of the intensity histogram of the single TMR and SF650 molecule (Fig. S3 *G* and *H*), the apparent number of D4H and TRPV4 molecules in each bright spot corresponds with 2 and 4 molecules at the peak of the intensity histograms, respectively (Fig. S3 *I* and *J*). The peak fluorescence intensities of the fast, medium, and immobile states of TRPV4 were approximately

Representative trajectories of TRPV4 molecules in each state, which colocalized with D4H (black). (*J*) Colocalization steps defined as the number of the colocalization trajectories of TRPV4 with D4H per second in the recorded movies and from 1 to 5 min after stimulation with the indicated condition (vehicle, 300 nM GSK101). Violin plots show the mean value and distribution of 20–22 cells. ***$p < 0.001$; **$p < 0.01$ with one-way ANOVA followed by the Tukey HSD test among four groups.

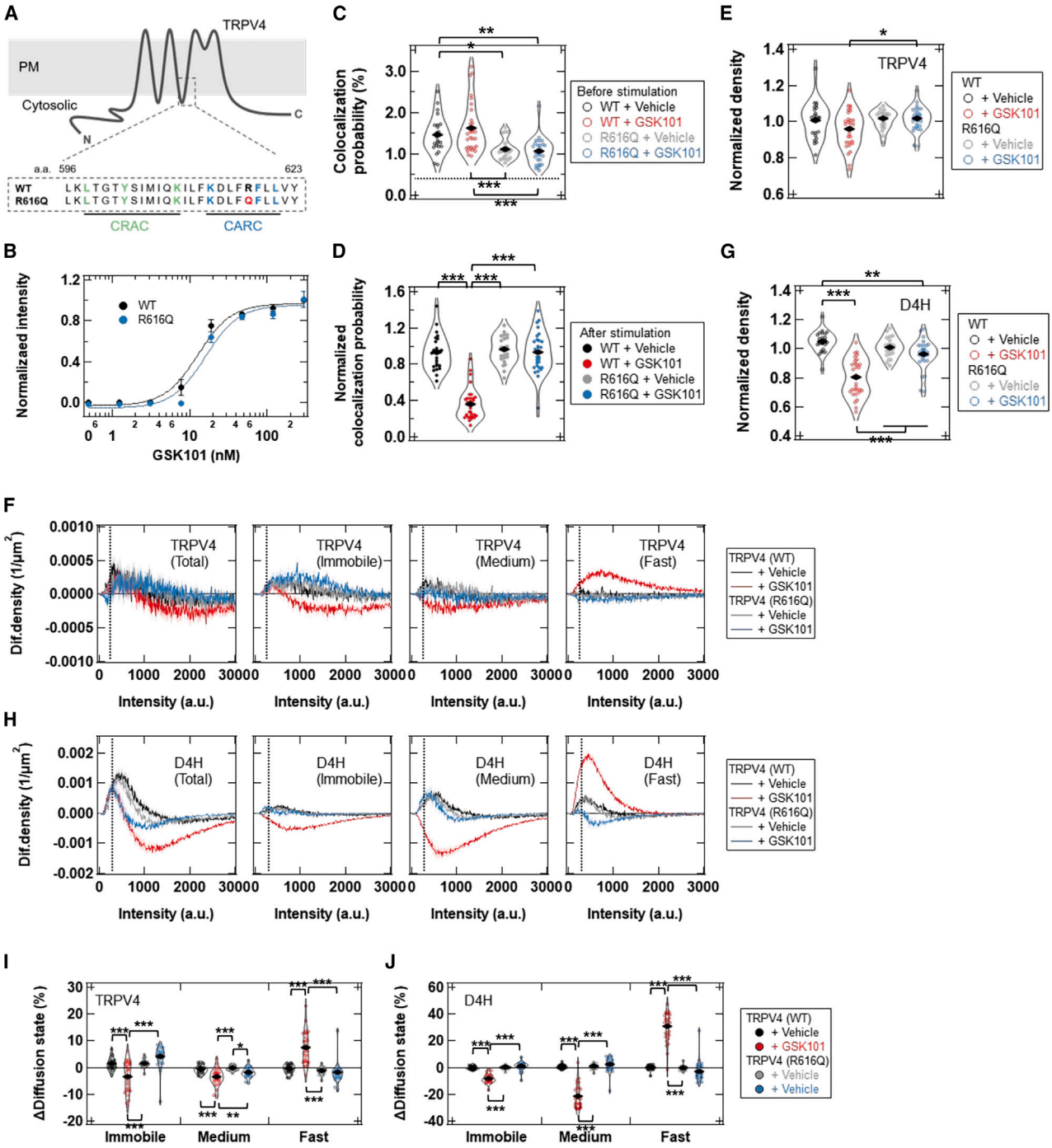

FIGURE 3 A cholesterol-binding motif of TRPV4 determines the D4H-accessible cholesterol behavior upon TRPV4 activation. (*A*) A scheme of the CRAC/CARC motif of TRPV4 and branchyolmia-causative R616Q mutation. (*B*) Dose-response curves of GSK101-induced Ca^{2+} influx in Halo-TRPV4 (WT, R616Q mutant)-expressing HeLa cells. Data are means ± SEM of three independent experiments. (*C*) Colocalization probability of TRPV4 (WT or R616Q mutant) molecules with D4H at the basal state before stimulation with the indicated condition (vehicle, 300 nM GSK101) was shown. The percentages represent the proportion of TRPV4 molecules colocalized with D4H to the total number of TRPV4 molecules. Violin plots show the mean value and distribution of 22–30 cells. *$p < 0.05$; **$p < 0.01$; ***$p < 0.001$ (one-way ANOVA followed by the Tukey honest significant difference [HSD] test among four groups). Dashed black line represents the false positive estimated from the random colocalization between SF650-labeled CD86 and TMR-labeled D4H (see also the left black circle of Fig. 1 *J*). (*D*) Colocalization probability of TRPV4 (WT or R616Q mutant) molecules with D4H from 1 to 5 min after GSK101 stimulation normalized to the basal state before stimulation. Violin plots show the mean value and distribution of 22–30 cells. ***$p < 0.001$ (one-way ANOVA followed by the Tukey HSD test among four groups). (*E–H*) Normalized density and histograms of density acquired by a dual-color single-molecule imaging of D4H and TRPV4 (WT or R616Q mutant). Density of TRPV4 (WT or R616Q mutant) (*E*) and D4H (*G*) from 1 to 5 min after stimulation with the indicated condition (vehicle, 300 nM GSK101) normalized to the basal state before stimulation was shown. Violin plots show the mean value and distribution

(legend continued on next page)

two, three, and four times the single SF650 molecule intensity, respectively (Fig. S3 *I*). The peak fluorescence intensities of the fast, medium, and immobile states of D4H were approximately one, two, and two times the single TMR molecule intensity, respectively (Fig. S3 *J*). Considering that the staining ratio of Halo-TRPV4 is approximately 60% (Fig. S3 *K*), fast-mobile TRPV4 molecules primarily form tetramers, while higher-order oligomers constitute the medium and immobile states. Conversely, for SNAP-D4H, the staining rate was less than 10% (Fig. S3 *L*), suggesting that the immobile and medium states arise from sampling the D4H-accessible cholesterol molecules forming nanoclusters.

TRPV4 activation reduces the D4H-accessible cholesterol nanocluster with lower mobility at the plasma membrane

We noticed that the fluorescence signal of D4H was decreased in the TIRF fields after HeLa cells were treated with GSK101 (Fig. 1 *D*, *F*, Videos S1 and S2), suggesting the effects of TRPV4 activation on plasmalemmal D4H-accessible cholesterol existence state. GSK101-mediated TRPV4 activation slightly reduced the particle density of TRPV4 molecules (Figs. 2 *C* and S3 *M*) and slightly increased its fast states (Fig. 2 *D*). Unexpectedly, treating HeLa cells with GSK101 significantly decreased the D4H particle density compared with vehicle treatment in TRPV4-expressing cells (Figs. 2 *E* and S3 *N*). Treatment of mock HeLa cells, in which TRPV4 plasmids were not transfected, with GSK101 did not affect the D4H particle density (Figs. 2 *E* and S3 *N*). TRPV4 activation apparently decreased D4H in its immobile and medium states and increased those in the fast state (Fig. 2 *F*), indicating that cluster size and diffusion coefficient are negatively correlated. Regarding the diffusion behavior of TRPV4 and D4H molecules upon GSK101 stimulation, we found that the diffusion coefficients and proportions of both TRPV4 and D4H molecules in the medium state were significantly decreased, accompanied by significant increases in the fast state (Figs. 2 *G*, *H*, S3 *O* and *P*). Then, we analyzed the diffusion states of TRPV4 molecules colocalized with D4H (Fig. 2 *I* and *J* and Videos S1 and S2). Before activation, TRPV4 was primarily colocalized with D4H in the immobile and medium states. Upon GSK101 stimulation, the frequency of TRPV4/D4H colocalization events in the immobile and medium states was significantly decreased. Collectively, these results, along with the fluorescence intensity histograms (Fig. 2 *D* and *F*), suggest that inactive TRPV4 molecules accumulated within the D4H-accessible cholesterol nanodomain. Active TRPV4 reduces the presence of D4H-accessible cholesterol nanoclusters surrounding it on the cytosolic plasma membrane leaflets, contributing to a reduction in the proportion of viscous membrane domains. This results in an increase in the fraction of fast-mobile TRPV4 and D4H-accessible cholesterol molecules.

Mutation in the CRAC/CARC motifs of TRPV4 attenuated GSK101-dependent alteration of D4H-accessible cholesterol dynamics

TRPV4 possesses a CRAC/CARC motif, a cholesterol-binding region between its transmembrane domain (TM) 4 and TM5, which is a hot spot of genetic mutations that cause skeletal dysplasia (Fig. 3 *A*) (27). Among them, $TRPV4^{R616Q}$ impairs complex formation with cholesterol *in vitro* (31). The calcium mobilization assay showed that the expression of $TRPV4^{R616Q}$ mutant induced Ca^{2+} influx by the stimulation of GSK101 as was seen in the expression of $TRPV4^{\text{wild-type (WT)}}$ (Fig. 3 *B*). To examine whether TRPV4 activation-dependent D4H-accessible cholesterol reduction requires the interaction between TRPV4 and D4H-accessible cholesterol, we performed dual-color single-molecule imaging of $TRPV4^{R616Q}$ and D4H. In the basal state, $TRPV4^{R616Q}$ significantly decreased colocalization with D4H compared with $TRPV4^{WT}$ (Fig. 3 *C*), suggesting that $TRPV4^{R616Q}$ is a loss-of-cholesterol interaction mutant. Upon GSK101 stimulation, no significant decrease in the colocalization probability between $TRPV4^{R616Q}$ and D4H was observed, unlike that with $TRPV4^{WT}$ (Fig. 3 *D*). The slight decrease in the particle density of $TRPV4^{WT}$ after GSK101 stimulation was significantly inhibited by the R616Q mutation (Fig. 3 *E*). The fast-mobile TRPV4 molecules did not increase when the $TRPV4^{R616Q}$-expressing cells were stimulated by GSK101 (Fig. 3 *F*). Remarkably, the GSK101-dependent reduction of D4H particle density in $TRPV4^{WT}$-expressing cells was completely suppressed in $TRPV4^{R616Q}$-expressing cells (Fig. 3 *G*). Although GSK101 stimulation increases the fast D4H molecules in $TRPV4^{WT}$-expressing cells, it did not increase the particle density histograms of D4H molecules in the fast state in $TRPV4^{R616Q}$-expressing cells (Fig. 3 *H*). The decrease of both TRPV4 and D4H molecules in the immobile and

of 22–30 cells. *p < 0.05; **p < 0.01; ***p < 0.001 (one-way ANOVA followed by the Tukey HSD test among four groups). The difference of density histograms in TRPV4 (WT or R616Q mutant) (*F*) and D4H (*H*) molecules before and from 1 to 5 min after stimulation with the indicated condition (vehicle, 300 nM GSK101) were shown. Dashed black lines represent the intensity of single molecules estimated from SF650-labeled CD86 (210 arbitrary units [a.u.]) and TMR-labeled CD86 (280 a.u.) (the monomeric control; see also Fig. S3 *G* and *H*). (*I*, *J*) Changes in the fractions in the diffusion states of TRPV4 (WT or R616Q mutant) (*I*) and D4H (*J*) molecules before and from 1 to 5 min after stimulation with the indicated condition (vehicle, 300 nM GSK101). Violin plots show the mean value and distribution of 22–30 cells. *p < 0.05; **p < 0.01; ***p < 0.001 (one-way ANOVA followed by the Tukey HSD test among 4 groups).

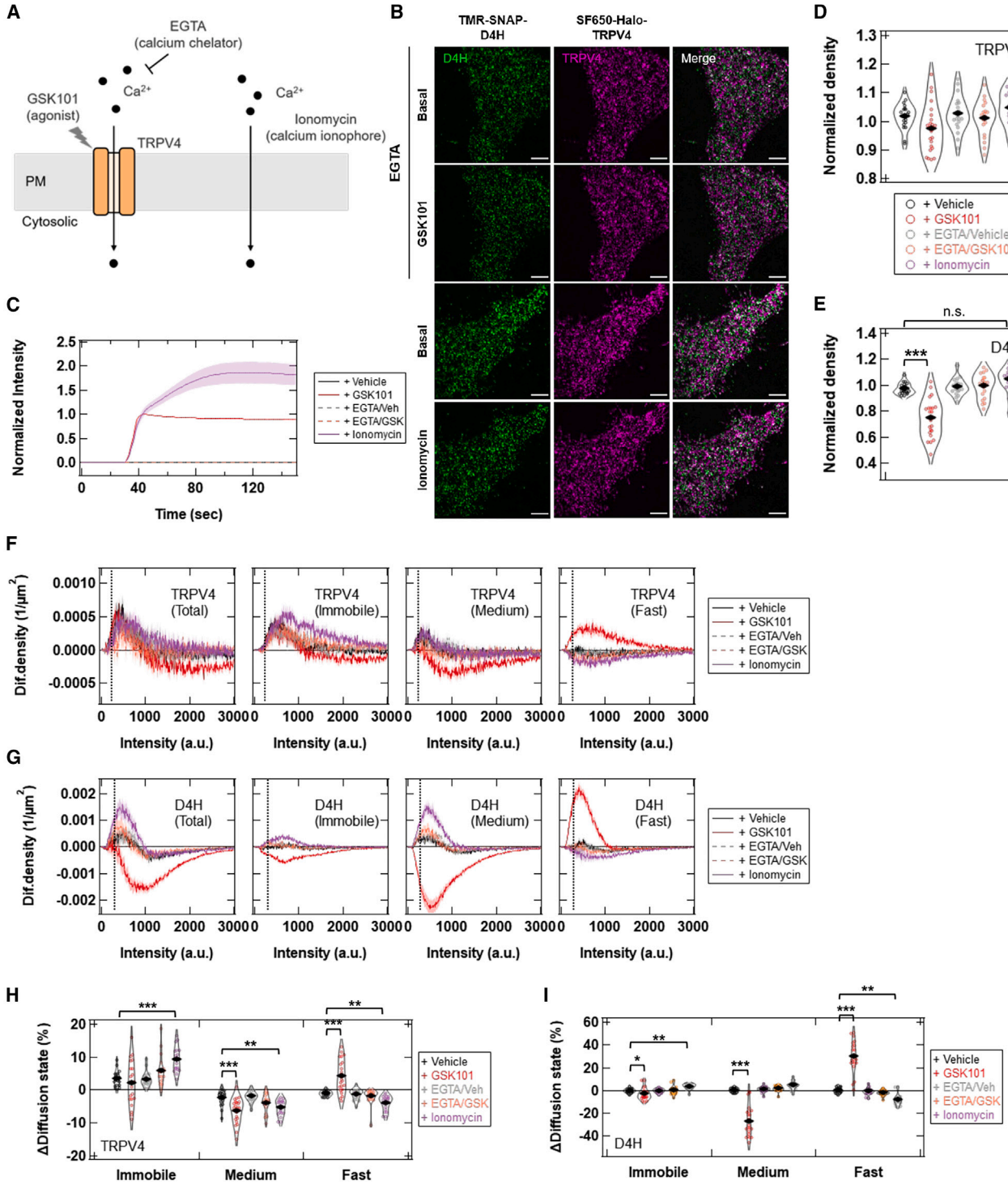

FIGURE 4 The alteration of D4H-accessible cholesterol dynamics requires TRPV4-mediated Ca^{2+} influx. (*A*) A scheme of the Ca^{2+} response measurement using EGTA and ionomycin in Fig. 4. (*B*) Representative total internal reflection fluorescence microscopy (TIRFM) images of TMR-labeled D4H (green) and SF650-labeled TRPV4 (magenta) at the basal state before stimulation and 5 min after 300 nM GSK101 stimulation in the presence of EGTA were shown in the top. Representative TIRFM images of cells at the basal state before stimulation and 5 min after 1 μM ionomycin stimulation were also shown in the bottom. Scale bars, 5 μm. (*C*) Representative Ca^{2+} influx in Halo-TRPV4-transfected HeLa cells under the indicated conditions. Lines and shaded regions represent mean and SEM of three independent experiments, respectively. (*D*, *E*) Density of TRPV4 (*D*) and D4H (*E*) from 1 to 5 min after stimulation with the indicated condition normalized to the basal state before stimulation was shown. Violin plots show the mean value and distribution of 19–22 cells. ***$p < 0.001$; n.s., not significant (one-way ANOVA followed by the Dunnett's test for multiple comparison analysis with reference to the vehicle). (*F*, *G*) The difference of density histograms in TRPV4 (*F*) and D4H (*G*) before and from 1 to 5 min after stimulation with the indicated

(legend continued on next page)

medium states and their increase in the fast state, which was observed in TRPV4^{WT}-expressing cells, were not observed in TRPV4^{R616Q}-expressing cells (Fig. 3 *I* and *J*). These results suggest that the interaction between TRPV4 and D4H-accessible cholesterol at the basal state is essential for altering plasmalemmal D4H-accessible cholesterol after TRPV4 activation.

TRPV4/D4H-accessible cholesterol interaction does not require their localization to caveolae

Since TRPV4 colocalized with D4H in the immobile and medium states (Fig. 2 *J*), we questioned whether cholesterol-rich membrane nanodomains were responsible for their interaction. As a previous study demonstrated that TRPV4 localizes in caveolae, cholesterol-rich domains at the plasma membrane (31), we investigated the involvement of caveolae in the TRPV4/D4H-accessible cholesterol interactions. We developed a triple-color single-molecule imaging of TMR-labeled D4H, SF650-labeled TRPV4$^{WT\ or\ R616Q}$, and EGFP-labeled Cav-1 (a marker of caveolae) in live HeLa cells (Fig. S4 *A* and Videos S3 and S4). The colocalization probability of TRPV4^{R616Q} with Cav-1 was almost identical to that of TRPV4^{WT} and was unaffected by GSK101 stimulation (Fig. S4 *B*). D4H and TRPV4 were observed to colocalize in the caveolae (Fig. S4 *C*; white dots indicated by blue arrows) and Cav-1-negative membrane domains (Fig. S4 *C*; magenta dots indicated by gray arrows). Thus, the interaction of TRPV4 with D4H-accessible cholesterol is not necessary for its localization at caveolae. We also found that the D4H in the immobile and medium states colocalized with Cav-1 (Fig. S4 *D*). Upon TRPV4 activation, the colocalization probability of Cav-1 molecules colocalized with D4H molecules was not significantly changed in TRPV4^{WT}- or TRPV4^{R616Q}-expressing cells (Fig. S4 *E*).

TRPV4-mediated Ca^{2+} influx and C-terminal CaM-binding site are necessary for the alteration of plasmalemmal D4H-accessible cholesterol dynamics

Finally, we elucidated the molecular mechanisms underlying the reduction of D4H particle density and the increase in D4H mobility at the plasma membrane upon TRPV4 activation. To examine the roles of TRPV4-mediated Ca^{2+} influx into the cytosol from the medium, we performed dual-color single-molecule imaging without extracellular Ca^{2+} using EGTA (a calcium chelator) or with ionomycin (a calcium ionophore) (Fig. 4 *A* and *B*). The calcium mobilization assay revealed that the TRPV4-mediated influx of Ca^{2+} into the cytosol was completely inhibited when HeLa cells were treated with EGTA, and ionomycin induced approximately twice as much Ca^{2+} influx as TRPV4 activation (Fig. 4 *C*). The decrease in particle density and increase in fast states of both TRPV4 and D4H molecules upon TRPV4 activation was not observed in the presence of EGTA (Fig. 4 *D*–*G*). The treatment of HeLa cells with ionomycin failed to reduce the particle density of TRPV4 and D4H molecules (Fig. 4 *D* and *E*). Ionomycin stimulation did not decrease the particle density of TRPV4 and D4H in immobile and medium states or increase their particle density in fast states, as seen after GSK101 stimulation (Fig. 4 *F* and *G*). Similarly, chelating extracellular Ca^{2+} using EGTA canceled the effects of TRPV4 activation on the proportion changes in TRPV4 and D4H molecules in each state (Fig. 4 *H* and *I*). Unlike GSK101 stimulation, treating the cells with ionomycin significantly increased the immobile fraction and decreased the fast fraction of both TRPV4 and D4H (Fig. 4 *H* and *I*). These results suggest that TRPV4-mediated Ca^{2+} influx increases the mobility of D4H-accessible cholesterol molecules at the cytosolic plasma membrane leaflets.

CaM forms a complex with Ca^{2+} and transduces various cellular signaling pathways (41). The C-terminal CaM-binding domain of TRPV4 (Fig. 5 *A*) interacts with CaM in a Ca^{2+}-dependent manner (4,42). To investigate whether the interaction of CaM with TRPV4 alters D4H-accessible cholesterol dynamics upon TRPV4 activation, we generated two "loss-of-CaM interaction TRPV4 mutants," TRPV4$^{\Delta 812\text{-}121}$ and TRPV4^{W822A} (Fig. 5 *A*) (4). The GSK101-induced Ca^{2+} influx of both mutants was similar to that of TRPV4^{WT} (Fig. 5 *B* and *C*). Then, we performed dual-color single-molecule imaging using those "loss-of-CaM interaction TRPV4 mutants" (Fig. 5 *D*). As shown in Fig. 5 *E* and *F*, the significant reduction in the particle density of TRPV4 and D4H molecules in TRPV4^{WT}-expressing cells upon TRPV4 activation was mitigated by the loss-of-CaM interaction TRPV4 mutants. Density histogram analysis showed that the GSK101-dependent decrease of TRPV4 and D4H in the immobile and medium states in TRPV4^{WT}-expressing cells was partially suppressed in TRPV4$^{\Delta 812\text{-}121}$- or TRPV4^{W822A}-expressing cells (Fig. 5 *G* and *H*). Regarding the population of TRPV4 and D4H, the GSK101-mediated increase and decrease in the fast state and immobile-state fraction of TRPV4 molecules, respectively, in TRPV4^{WT}-expressing cells were significantly suppressed by expression of the loss-of-CaM interaction TRPV4 mutants instead of TRPV4^{WT} (Fig. 5 *I*). The GSK101-mediated increase in the fast state fraction and decrease in the medium state fraction of D4H molecules in

condition. Dashed black lines represent the intensity of single molecules estimated from SF650-labeled CD86 (210 arbitrary units [a.u.]) and TMR-labeled CD86 (280 a.u.) (the monomeric control; see also Fig. S3 *G* and *H*). (*H*, *I*) Changes in the fractions in the diffusion states of TRPV4 (*H*) and D4H (*I*) molecules before and from 1 to 5 min after stimulation with the indicated condition. Violin plots show the mean value and distribution of 19–22 cells. *$p < 0.05$; **$p < 0.01$; ***$p < 0.001$ with one-way ANOVA followed by the Dunnett's test for multiple comparison analysis with reference to the vehicle.

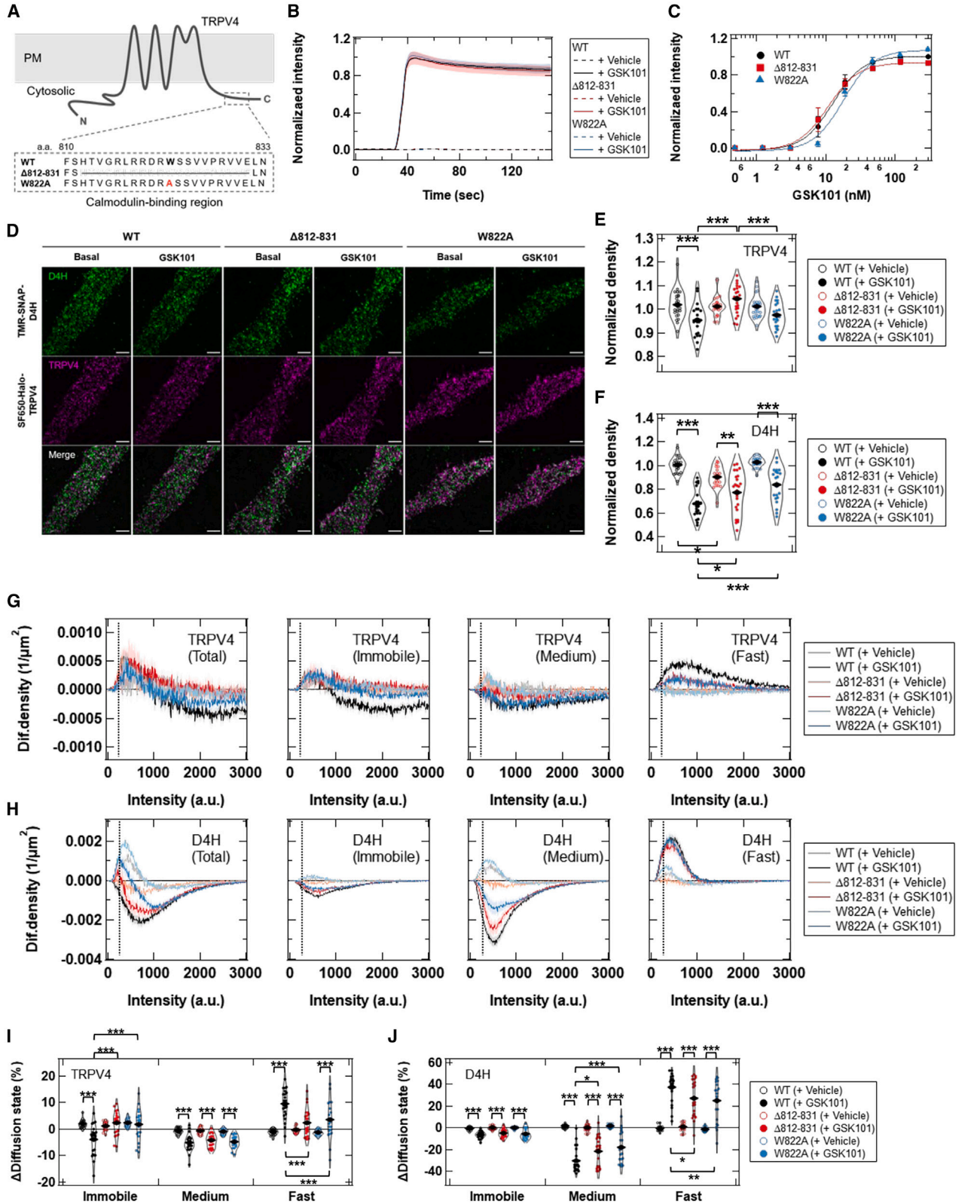

FIGURE 5 A CaM-binding site was partially required for the changes in D4H-accessible cholesterol dynamics. (*A*) A scheme of the CaM-binding site. (*B*) Representative Ca^{2+} influx in Halo-TRPV4 (WT, Δ812-831 mutant, and W822A mutant)-expressing HeLa cells under the indicated conditions (vehicle, 300 nM GSK101). Lines and shaded regions represent mean and SEM of three independent experiments, respectively. (*C*) Dose-response curves of GSK101 in Halo-TRPV4 (WT, Δ812-831 mutant, and W822A mutant)-expressing HeLa cells. Data are means ± SEM of three independent experiments.

(legend continued on next page)

$TRPV4^{WT}$-expressing cells were partially, but significantly attenuated in the loss-of-CaM interaction TRPV4 mutants-expressing cells (Fig. 5 *J*). Collectively, these results suggest that the interaction of CaM with TRPV4 partially contributes to the alterations in TRPV4 and D4H-accessible cholesterol behavior at the plasma membrane, which is induced by TRPV4-mediated Ca^{2+} influx.

The increase in cytosolic Ca^{2+} concentration can activate phospholipid scramblases, which causes the phospholipid scrambling leading to the exposure of PS to the cell surface (43). We thus assessed the effects of TRPV4-mediated Ca^{2+} influx on PS exposure by annexin V staining. We found that GSK101 stimulation induced the PS exposure within 5 min (a similar time course of single-molecule imaging in this study) in both $TRPV4^{WT}$- and $TRPV4^{R616Q}$-expressing cells (Fig. S5 *A* and *B*; arrows). In $TRPV4^{R616Q}$-expressing cells, although GSK101 stimulation induced Ca^{2+} influx (Fig. 3 *B*) and the PS exposure (Fig. S5 *B*; arrows) as in $TRPV4^{WT}$-expressing cells, the alteration of D4H-accessible cholesterol dynamics was not observed upon TRPV4 activation (Fig. 3 *C*–*J*). The binding of D4H to cholesterol in liposomes containing 30 mol% or 60 mol% cholesterol was not affected by the presence of 20 mol% PS, a similar amount of PS at the cytosolic leaflets of the plasma membrane (20). Together, these results suggest that the interaction between D4H-accessible cholesterol and TRPV4, rather than the PS and other phospholipids scrambling, is important for the alteration of D4H-accessible cholesterol dynamics caused by the TRPV4-mediated Ca^{2+} influx.

DISCUSSION

In this study, we propose a model for the spatiotemporal interaction between TRPV4 and D4H-accessible cholesterol at the plasma membrane (Fig. 6). In the basal state, TRPV4 associates with D4H-accessible cholesterol in the low fluidity plasma membrane domains via its CRAC/CARC motif, in which TRPV4 and D4H-accessible cholesterol are highly clustered (Fig. 6; left). Once TRPV4 is activated by its agonist, TRPV4-mediated Ca^{2+} influx triggers the reduction of plasmalemmal D4H-accessible cholesterol clusters, which partially depends on CaM-binding (Fig. 6; middle). The decrease in D4H-accessible cholesterol clusters generates high-fluidity plasma membrane domains, which promotes the diffusion of TRPV4 and D4H-accessible cholesterol, reducing their interaction at the plasma membrane (Fig. 6; right). Canonically, cholesterol acts as a platform to form cholesterol-rich nanodomains (e.g., lipid rafts) with sphingolipids and glycolipids to control various membrane proteins (19,44). In contrast, several recent studies suggest that the activities of membrane proteins cooperate with the local membrane lipid environment. Ligand-induced EGFR autophosphorylation regulates molecular assembly and signaling in cooperation with cholesterol and anionic phospholipid molecules (45,46). Since each TRPV4 subunit should bind to cholesterol in a 1:1 stoichiometry, TRPV4 might affect the surrounding cholesterol molecules. Here, we unexpectedly discovered that the TRPV4 activation reduces the clusters of D4H-accessible cholesterol molecules and increases their mobility at the plasma membrane. These effects of the TRPV4 activation on plasmalemmal cholesterol dynamics is global, although it is expected that TRPV4 affects its boundary local cholesterol considering a 1:1 stoichiometry of the TRPV4/cholesterol interaction. We propose that the TRPV4 can control the extensive membrane lipid environments.

Physiologically, TRPV4 is essential for the differentiation of osteoclasts and their functions (47,48). Genetic ablation of the *TRPV4* gene impairs bone resorption activities of osteoclasts, leading to increased bone mass (47). We found that $TRPV4^{WT}$-mediated Ca^{2+} influx changes the behavior of plasmalemmal D4H-accessible cholesterol (Fig. 2 *E*, *F*, and *H*). The introduction of an R616Q mutation in the CRAC/CARC motif of TRPV4 causes branchyolmia, which is characterized by a short trunk, scoliosis, and mild short stature (28). $TRPV4^{R616Q}$ acts as a gain-of-function mutant possessing high Ca^{2+} influx capacity, which promotes osteoclast proliferation, resulting in backbone abnormality (28,49,50). Our results indicate that $TRPV4^{R616Q}$ activation fails to alter the plasmalemmal D4H-accessible cholesterol dynamics because of the loss of interaction with cholesterol (Fig. 3 *G*, *H* and *J*). Therefore, $TRPV4^{R616Q}$ might cause the onset of skeletal disease by dysregulating cholesterol behavior at the plasma membrane. The removal of cholesterol from the plasma membrane by MβCD suppresses the differentiation, maturation, and survival of osteoclasts (51–53). Deletion of low-density lipoprotein receptors inhibits osteoclast formation due to the improper localization of proteins that regulate cell-cell fusion of preosteoclasts (54). Together, osteoclasts require plasmalemmal

(*D*) Representative total internal reflection fluorescence microscopy (TIRFM) images of TMR-labeled D4H (green) and SF650-labeled TRPV4 (WT, Δ812-831 mutant, or W822A mutant; magenta) at the basal state before stimulation and 5 min after 300 nM GSK101 stimulation. Scale bars, 5 μm. (*E*, *F*) Density of TRPV4 (WT, Δ812-831 mutant or W822A mutant) (*E*) and D4H (F) from 1 to 5 min after stimulation with the indicated condition (vehicle, 300 nM GSK101) normalized to the basal state before stimulation. Violin plots show the mean value and distribution of 21–26 cells. *$p < 0.05$; **$p < 0.01$; ***$p < 0.001$ with one-way ANOVA followed by the Tukey honest significant difference (HSD) test among six groups. (*G*, *H*) The difference of density histograms in TRPV4 (WT, Δ812-831 mutant or W822A mutant) (*G*) and D4H (*H*) before and from 1 to 5 min after stimulation with the indicated condition (vehicle, 300 nM GSK101). Dashed black lines represent the intensity of single molecules estimated from SF650-labeled CD86 (210 arbitrary units [a.u.]) and TMR-labeled CD86 (280 a.u.) (the monomeric control; see also Fig. S3 *G* and *H*). (*I*, *J*) Changes in the fractions in the diffusion states of TRPV4 (*I*) and D4H (*J*) molecules before and from 1 to 5 min after stimulation with the indicated condition (vehicle, 300 nM GSK101). Violin plots show the mean value and distribution of 21–26 cells. *$p < 0.05$; **$p < 0.01$; ***$p < 0.001$ with one-way ANOVA followed by the Tukey HSD test among 6 groups.

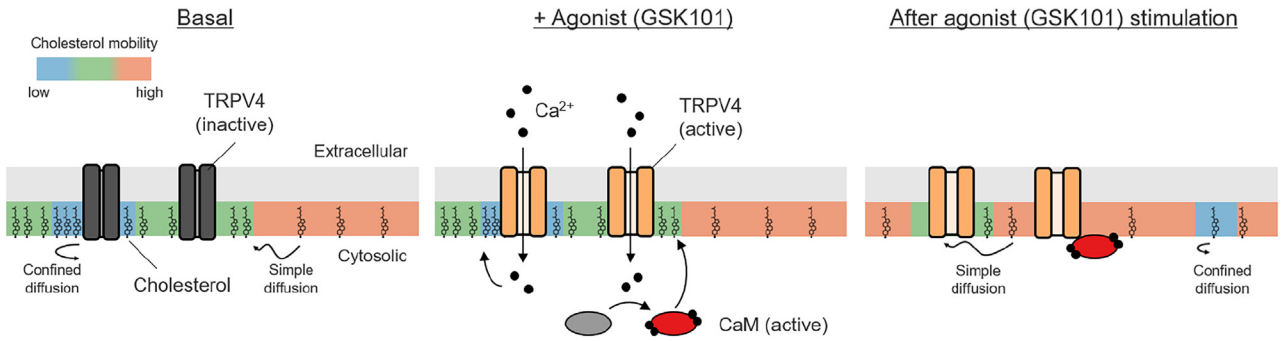

FIGURE 6 Model of the spatiotemporal interaction between TRPV4 and cholesterol at the plasma membrane. In the basal state, TRPV4 associates with cholesterol exhibiting the confined diffusion at the plasma membrane, in which TRPV4 and cholesterol are highly clustered (left). TRPV4 rarely interacts with cholesterol exhibiting the simple diffusion in the basal state (left). Upon TRPV4 activation by its agonist (GSK101), TRPV4-mediated local Ca^{2+} influx into cytosol causes the reduction of cholesterol nanoclusters with lower mobility and an increase in fast-mobile cholesterol, which is partially dependent on CaM (middle). After TRPV4 activation, the generation of high-fluidity plasmalemmal nanodomains due to the decrease of cholesterol nanoclusters increases the diffusion of both TRPV4 and cholesterol molecules, which reduces their interaction at the plasma membrane (right).

cholesterol for their proper differentiation, maturation, and survival. Therefore, TRPV4 might contribute to osteoclast differentiation by regulating intracellular calcium concentration and the cholesterol state at the plasma membrane.

Since the fluorophores at the cell surface are selectively excited in a TIRF microscopy, the fluorescence intensity of molecules is susceptible to the distance from the coverslips, which could be affected by cell morphological changes. Brighter D4H spots in the image could not only reflect the elevated amount of cholesterol, but also correspond with areas with irregular membrane morphology that mimics D4H clusters. Given the latter case, the conversion of the nonflat region to a flat region would increase the apparent membrane area after the TRPV4 activation. As shown in Fig. S2 *O* and *P*, GSK101 stimulation did not increase the apparent membrane area. If the membrane morphology was changed by TRPV4 activation, not only the intensity of D4H, but also that of TRPV4, could be affected. In the same cell, the changes in the TRPV4 fluorescence signals were slight compared with that in the D4H fluorescence signals upon TRPV4 activation (Fig. 2 *C* and *E*). These results suggest that it is not likely that morphological changes of the plasma membrane by TRPV4 activation affect the particle density of D4H.

In the present study, because we transiently expressed TRPV4 in D4H-stably expressing HeLa cells, the expression levels of TRPV4 at the plasma membrane may vary among cells in a series of experiments. The labeling condition is the same throughout all experiments in this study. As shown in Fig. S3 *M*, the mean particle density of TRPV4 before vehicle stimulation and before GSK101 stimulation was less than 0.1 particle/μm^2. The difference in the mean particle density of TRPV4 was not observed before stimulations (Fig. S4 *F*; vehicle stimulation [black circle] versus GSK101 stimulation [red circle]). Additionally, the distribution of spot density of D4H at the basal state remains constant across various experimental conditions (Figs. S3 *N* and S4 *G*). Since we are only focusing on the differences between the effects of vehicle and GSK101 stimulations, these factors would not have a significant impact on our conclusions.

Due to a hydrophobic feature of GSK101, the agonist may diffuse quickly in cellular membranes, perturb their structural order, and alter their mechanical, electrical, and thermodynamic membrane properties. The behavior of D4H-accessible cholesterol after GSK101 treatment was changed in neither $TRPV4^{R616Q}$-expressing HeLa cells nor TRPV4-untransfected HeLa cells, in which TRPV4 plasmids were not transfected (Figs. 2 *E*, S3 *N* and *P*). These results suggest no intrinsic implication of GSK101 in the D4H-accessible cholesterol dynamics. Not only GSK101 but also various other stimuli (e.g., temperature, shear stress) are capable of activating TRPV4 and eliciting Ca^{2+} influx. Given that temperature also influences membrane biophysical properties, the relationships between temperature, TRPV4 activities and cholesterol behaviors will be investigated in future.

Our results indicated that TRPV4-mediated Ca^{2+} influx is essential for the alteration of plasmalemmal D4H-accessible cholesterol dynamics. Mechanistically, we showed that the C-terminal CaM-binding site of TRPV4, which can interact with tubulins leading to the formation of a complex, including Annexin A2 (AnxA2) (55,56), partially contributes to this phenotype. A cholesterol-rich membrane is required for the plasmalemmal recruitment of AnxA2 (57,58). AnxA2 reduces cholesterol aggregation and membrane ordering in the presence of Ca^{2+} (59,60). The molecular machinery by which TRPV4-mediated Ca^{2+} influx, including CaM and AnxA2, alters cholesterol dynamics should be further investigated. The increase in Ca^{2+} concentration in the cytosol activates phospholipid scramblases (43). GSK101-mediated Ca^{2+} influx through TRPV4 triggers TMEM16F activation, resulting in the PS exposure in trophoblasts (61). We showed that, at least, the phospholipid scrambling and PS exposure caused by TRPV4-mediated Ca^{2+} influx was not associated with the alteration of

D4H-accessible cholesterol dynamics (Figs. 3 *G*, *H*, *J*, S5 *A* and *B*). The behavior of plasmalemmal D4H-accessible cholesterol can be explored in detail using dual-color, single-molecule imaging of D4H and other membrane proteins, which manipulate intracellular Ca^{2+} influx (e.g., other TRP channels, Piezo channels, Gq protein-coupled GPCRs [G-protein coupled receptor]).

Here, we used D4H to visualize cholesterol at the cytosolic plasma membrane leaflet, considering the transmembrane positioning of the CRAC/CARC motif in TRPV4. D4H is originally generated by the introduction of a D434S mutation into the D4 domain, a cholesterol-binding domain of PFO, which decreases the threshold for cholesterol binding to 20 mol% (20). PFO interacts with cholesterol at the exofacial leaflets of the plasma membrane, leading to their oligomerization and the pore formation with its D1, D2, and D3 domains followed by cell lysis (62,63). A threonine-leucine (T490-L491) pair in the loop L1 in D4 is critical for the recognition of membrane cholesterol (64). The crystal structure of PFO predicts a 1:1 stoichiometry in the binding of PFO and cholesterol (65), suggesting the same stoichiometry in the D4H/cholesterol interaction. The model of PFO and cholesterol interaction proposes that PFO recognizes the 3 β-OH and hydrophobic moiety of cholesterol (65). *In silico* homology modeling of the TRPV4-cholesterol interaction suggested that TRPV4 associates with cholesterol *via* electrostatic and hydrophobic interaction (31). These results suggest that the interaction of cholesterol with TRPV4 could interfere with the binding D4H to plasmalemmal cholesterol. Consequently, cholesterol labeled with D4H may represent free cholesterol, but not TRPV4-bound cholesterol. Because the binding curve of D4H to membrane cholesterol is nonlinear (20), a modest decrease in cholesterol concentration at the cytosolic leaflets of the plasma membrane may cause a large decrease in D4H particle density. The binding affinity of D4H to cholesterol-containing liposomes is decreased in the presence of SM (66). In contrast, at least 20 mol% PS does not affect the binding of D4H to 30 mol% or 60 mol% cholesterol-containing liposomes (20). The effects of the surrounding membrane environment on D4H-accessible cholesterol dynamics could be investigated by manipulating the plasmalemmal lipid compositions. The membrane cholesterol can be classified into three distinct pools: PFO-accessible, SM-sequestered, and residual pools based on the accessibility of PFO (67). The PFO-accessible pool is depleted when cells are treated with MβCD (62,67). Since D4H is a mutant of the D4 domain of PFO (32) and plasmalemmal D4H signals are diminished by MβCD (Fig. 1 *B* and *C*), D4H-accessible cholesterol is equivalent to PFO-accessible cholesterol. Although we characterized the behavior of D4H-accessible cholesterol upon TRPV4 activation, the characteristics of other two cholesterol pools during TRPV4 activation as well as their interactions with TRPV4 are unclear. TRPV4 activation reduced D4H-accessible cholesterol molecules at the cytosolic leaflets of the plasma membrane (Fig. 2 *E*), which might be converted to an SM-sequestered pool and/or a residual pool, or an internalized into intracellular compartments from the plasma membrane by the TRPV4 activation. By the addition of SM-sequestered cholesterol probes (e.g., Ostreolysin A (68), Nakanori (69)) in the media, the SM-sequestered pool at the exofacial leaflets of the plasma membrane can be visualized. Combining these probes with D4H may help to reveal the transition of cholesterol states at the plasma membrane upon TRPV4 activation.

CONCLUSIONS

We successfully visualized the colocalization of TRPV4 with D4H-accessible cholesterol via its cholesterol-interacting motif at the cytosolic plasma membrane leaflet in live cells. Dual-color single-molecule imaging analysis uncovered that TRPV4-mediated Ca^{2+} influx reduced the particle density and increased the mobility of D4H-accessible cholesterol molecules, partially involving the C-terminal CaM-binding site of TRPV4. The binding of cholesterol to TRPV4 was essential for altering the plasmalemmal D4H-accessible cholesterol behavior upon agonist-evoked TRPV4 activation. We thus propose a new role of TRPV4-mediated Ca^{2+} influx as a remodeling factor of cholesterol dynamics at the cytosolic plasma membrane leaflets.

SUPPORTING MATERIAL

Supporting material can be found online at https://doi.org/10.1016/j.bpj.2024.02.030.

AUTHOR CONTRIBUTIONS

Y.S. and M.A. conceptualized and supervised this project. Y.K. designed and performed all experiments, statistical analyses, data visualizations, and figure illustrations. M.Y. developed the program of single-molecule analysis. M.Abe provided the cDNA for TRPV4 and D4H, the plasmid of EGFP-PLCδ-PH. Y.K., M.Y., and M.Maekawa wrote and revised the manuscript with contributions from all the authors.

ACKNOWLEDGMENTS

We thank Dr. Masato Yasui (ZIDO corp.) for technical support on the trajectory simulation. This work was supported by the Keio University Doctoral Student Grant-in-Aid Program from the Ushioda Memorial Fund and MEXT Japan with Grants-in-Aid for JSPS Fellows (23KJ1891) to Y.K., JSPS KAKENHI (19H05647) and by JST PRESTO (JPMJPR20EF) to M.Y., JST CREST (JPMJCR1912) to Y.S., RIKEN Pioneering Project "Glyco-Lipidologue Initiative" to Y.S. and M.A., and JSPS KAKENHI (20H00495) and JST ERATO "Arita Lipidome Atlas Project" (JPMJER2101) to M.A.

DECLARATION OF INTERESTS

The authors declare no competing interests.

REFERENCES

1. White, J. P. M., M. Cibelli, …, I. Nagy. 2016. TRPV4: Molecular Conductor of a Diverse Orchestra. *Physiol. Rev.* 96:911–973. https://doi.org/10.1152/physrev.00016.2015.
2. Nilius, B., and T. Voets. 2013. The puzzle of TRPV4 channelopathies. *EMBO Rep.* 14:152–163. https://doi.org/10.1038/embor.2012.219.
3. Deng, Z., N. Paknejad, …, P. Yuan. 2018. Cryo-EM and X-ray structures of TRPV4 reveal insight into ion permeation and gating mechanisms. *Nat. Struct. Mol. Biol.* 25:252–260. https://doi.org/10.1038/s41594-018-0037-5.
4. Strotmann, R., G. Schultz, and T. D. Plant. 2003. Ca2+-dependent potentiation of the nonselective cation channel TRPV4 is mediated by a C-terminal calmodulin binding site. *J. Biol. Chem.* 278:26541–26549. https://doi.org/10.1074/jbc.M302590200.
5. Cordero-Morales, J. F., and V. Vásquez. 2018. How lipids contribute to ion channel function, a fat perspective on direct and indirect interactions. *Curr. Opin. Struct. Biol.* 51:92–98. https://doi.org/10.1016/j.sbi.2018.03.015.
6. Takahashi, N., S. Hamada-Nakahara, …, S. Suetsugu. 2014. TRPV4 channel activity is modulated by direct interaction of the ankyrin domain to PI(4,5)P(2). *Nat. Commun.* 5:4994. https://doi.org/10.1038/ncomms5994.
7. Caires, R., F. J. Sierra-Valdez, …, J. F. Cordero-Morales. 2017. Omega-3 Fatty Acids Modulate TRPV4 Function through Plasma Membrane Remodeling. *Cell Rep.* 21:246–258. https://doi.org/10.1016/j.celrep.2017.09.029.
8. Zhu, Y., L. Wen, …, X. Ma. 2021. Omega-3 fatty acids improve flow-induced vasodilation by enhancing TRPV4 in arteries from diet-induced obese mice. *Cardiovasc. Res.* 117:2450–2458. https://doi.org/10.1093/cvr/cvaa296.
9. Caires, R., T. A. C. Garrud, …, J. F. Cordero-Morales. 2022. Genetic- and diet-induced omega-3 fatty acid enrichment enhances TRPV4-mediated vasodilation in mice. *Cell Rep.* 40, 111306. https://doi.org/10.1016/j.celrep.2022.111306.
10. Lakk, M., O. Yarishkin, …, D. Križaj. 2017. Cholesterol regulates polymodal sensory transduction in Muller glia. *Glia.* 65:2038–2050. https://doi.org/10.1002/glia.23213.
11. Lakk, M., G. F. Hoffmann, …, D. Križaj. 2021. Membrane cholesterol regulates TRPV4 function, cytoskeletal expression, and the cellular response to tension. *J. Lipid Res.* 62, 100145. https://doi.org/10.1016/j.jlr.2021.100145.
12. Chen, Y. L., and S. K. Sonkusare. 2020. Endothelial TRPV4 channels and vasodilator reactivity. *Curr. Top. Membr.* 85:89–117. https://doi.org/10.1016/bs.ctm.2020.01.007.
13. Ikonen, E. 2008. Cellular cholesterol trafficking and compartmentalization. *Nat. Rev. Mol. Cell Biol.* 9:125–138. https://doi.org/10.1038/nrm2336.
14. Lange, Y., M. H. Swaisgood, …, T. L. Steck. 1989. Plasma Membranes Contain Half the Phospholipid and 90% of the Cholesterol and Sphingomyelin in Cultured Human Fibroblasts. *J. Biol. Chem.* 264:3786–3793. https://doi.org/10.1016/s0021-9258(19)84918-9.
15. Gagescu, R., N. Demaurex, …, J. Gruenberg. 2000. The recycling endosome of Madin-Darby canine kidney cells is a mildly acidic compartment rich in raft components. *Mol. Biol. Cell.* 11:2775–2791. https://doi.org/10.1091/mbc.11.8.2775.
16. van Meer, G., D. R. Voelker, and G. W. Feigenson. 2008. Membrane lipids: where they are and how they behave. *Nat. Rev. Mol. Cell Biol.* 9:112–124. https://doi.org/10.1038/nrm2330.
17. Doktorova, M., J. L. Symons, and I. Levental. 2020. Structural and functional consequences of reversible lipid asymmetry in living membranes. *Nat. Chem. Biol.* 16:1321–1330. https://doi.org/10.1038/s41589-020-00688-0.
18. Kusumi, A., T. A. Tsunoyama, …, K. G. N. Suzuki. 2023. Cholesterol- and actin-centered view of the plasma membrane: updating the Singer-Nicolson fluid mosaic model to commemorate its 50th anniversary(†). *Mol. Biol. Cell.* 34, pl1. https://doi.org/10.1091/mbc.E20-12-0809.
19. Lingwood, D., and K. Simons. 2010. Lipid rafts as a membrane-organizing principle. *Science.* 327:46–50. https://doi.org/10.1126/science.1174621.
20. Maekawa, M., and G. D. Fairn. 2015. Complementary probes reveal that phosphatidylserine is required for the proper transbilayer distribution of cholesterol. *J. Cell Sci.* 128:1422–1433. https://doi.org/10.1242/jcs.164715.
21. Raghupathy, R., A. A. Anilkumar, …, S. Mayor. 2015. Transbilayer lipid interactions mediate nanoclustering of lipid-anchored proteins. *Cell.* 161:581–594. https://doi.org/10.1016/j.cell.2015.03.048.
22. Cho, K. J., D. van der Hoeven, …, J. F. Hancock. 2016. Inhibition of Acid Sphingomyelinase Depletes Cellular Phosphatidylserine and Mislocalizes K-Ras from the Plasma Membrane. *Mol. Cell Biol.* 36:363–374. https://doi.org/10.1128/MCB.00719-15.
23. Hirama, T., R. Das, …, G. D. Fairn. 2017. Phosphatidylserine dictates the assembly and dynamics of caveolae in the plasma membrane. *J. Biol. Chem.* 292:14292–14307. https://doi.org/10.1074/jbc.M117.791400.
24. Parton, R. G., and M. A. del Pozo. 2013. Caveolae as plasma membrane sensors, protectors and organizers. *Nat. Rev. Mol. Cell Biol.* 14:98–112. https://doi.org/10.1038/nrm3512.
25. Fantini, J., and F. J. Barrantes. 2013. How cholesterol interacts with membrane proteins: an exploration of cholesterol-binding sites including CRAC, CARC, and tilted domains. *Front. Physiol.* 4:31. https://doi.org/10.3389/fphys.2013.00031.
26. Fantini, J., C. Di Scala, …, F. J. Barrantes. 2016. Molecular mechanisms of protein-cholesterol interactions in plasma membranes: Functional distinction between topological (tilted) and consensus (CARC/CRAC) domains. *Chem. Phys. Lipids.* 199:52–60. https://doi.org/10.1016/j.chemphyslip.2016.02.009.
27. Kumari, S., A. Kumar, …, C. Goswami. 2015. Influence of membrane cholesterol in the molecular evolution and functional regulation of TRPV4. *Biochem. Biophys. Res. Commun.* 456:312–319. https://doi.org/10.1016/j.bbrc.2014.11.077.
28. Rock, M. J., J. Prenen, …, D. H. Cohn. 2008. Gain-of-function mutations in TRPV4 cause autosomal dominant brachyolmia. *Nat. Genet.* 40:999–1003. https://doi.org/10.1038/ng.166.
29. Nishimura, G., J. Dai, …, A. Superti-Furga. 2010. Spondylo-epiphyseal dysplasia, Maroteaux type (pseudo-Morquio syndrome type 2), and parastremmatic dysplasia are caused by TRPV4 mutations. *Am. J. Med. Genet.* 152A:1443–1449. https://doi.org/10.1002/ajmg.a.33414.
30. Teng, J., A. Anishkin, …, P. Blount. 2019. Human mutations highlight an intersubunit cation-pi bond that stabilizes the closed but not open or inactivated states of TRPV channels. *Proc. Natl. Acad. Sci. USA.* 116:9410–9416. https://doi.org/10.1073/pnas.1820673116.
31. Das, R., and C. Goswami. 2019. TRPV4 expresses in bone cell lineages and TRPV4-R616Q mutant causing Brachyolmia in human reveals "loss-of-interaction" with cholesterol. *Biochem. Biophys. Res. Commun.* 517:566–574. https://doi.org/10.1016/j.bbrc.2019.07.042.
32. Maekawa, M. 2017. Domain 4 (D4) of Perfringolysin O to Visualize Cholesterol in Cellular Membranes-The Update. *Sensors.* 17, 504. https://doi.org/10.3390/s17030504.
33. Kuwashima, Y., M. Yanagawa, …, Y. Sako. 2021. Comparative Analysis of Single-Molecule Dynamics of TRPV1 and TRPV4 Channels in Living Cells. *Int. J. Mol. Sci.* 22, 8473. https://doi.org/10.3390/ijms22168473.
34. Kawakami, K., M. Yanagawa, …, A. Inoue. 2022. Heterotrimeric Gq proteins act as a switch for GRK5/6 selectivity underlying beta-arrestin transducer bias. *Nat. Commun.* 13:487. https://doi.org/10.1038/s41467-022-28056-7.
35. Mortensen, K. I., L. S. Churchman, …, H. Flyvbjerg. 2010. Optimized localization analysis for single-molecule tracking and super-resolution microscopy. *Nat. Methods.* 7:377–381. https://doi.org/10.1038/nmeth.1447.
36. Yanagawa, M., and Y. Sako. 2021. Workflows of the Single-Molecule Imaging Analysis in Living Cells: Tutorial Guidance to the Measurement of

the Drug Effects on a GPCR. *Methods Mol. Biol.* 2274:391–441. https://doi.org/10.1007/978-1-0716-1258-3_32.

37. Koyama-Honda, I., K. Ritchie, …, A. Kusumi. 2005. Fluorescence imaging for monitoring the colocalization of two single molecules in living cells. *Biophys. J.* 88:2126–2136. https://doi.org/10.1529/biophysj.104.048967.
38. Nishiguchi, T., H. Yoshimura, …, T. Ozawa. 2020. Synergetic Roles of Formyl Peptide Receptor 1 Oligomerization in Ligand-Induced Signal Transduction. *ACS Chem. Biol.* 15:2577–2587. https://doi.org/10.1021/acschembio.0c00631.
39. Yanagawa, M., M. Hiroshima, …, Y. Sako. 2018. Single-molecule diffusion-based estimation of ligand effects on G protein-coupled receptors. *Sci. Signal.* 11, eaao1917. https://doi.org/10.1126/scisignal.aao1917.
40. Calebiro, D., F. Rieken, …, M. J. Lohse. 2013. Single-molecule analysis of fluorescently labeled G-protein-coupled receptors reveals complexes with distinct dynamics and organization. *Proc. Natl. Acad. Sci. USA.* 110:743–748. https://doi.org/10.1073/pnas.1205798110.
41. Chin, D., and A. R. Means. 2000. Calmodulin: a prototypical calcium sensor. *Trends Cell Biol.* 10:322–328. https://doi.org/10.1016/s0962-8924(00)01800-6.
42. Loukin, S. H., J. Teng, and C. Kung. 2015. A channelopathy mechanism revealed by direct calmodulin activation of TrpV4. *Proc. Natl. Acad. Sci. USA.* 112:9400–9405. https://doi.org/10.1073/pnas.1510602112.
43. Suzuki, J., T. Fujii, …, S. Nagata. 2013. Calcium-dependent phospholipid scramblase activity of TMEM16 protein family members. *J. Biol. Chem.* 288:13305–13316. https://doi.org/10.1074/jbc.M113.457937.
44. Kim, D. H., H. M. Triet, and S. H. Ryu. 2021. Regulation of EGFR activation and signaling by lipids on the plasma membrane. *Prog. Lipid Res.* 83, 101115. https://doi.org/10.1016/j.plipres.2021.101115.
45. Hiroshima, M., C. G. Pack, …, Y. Sako. 2018. Transient Acceleration of Epidermal Growth Factor Receptor Dynamics Produces Higher-Order Signaling Clusters. *J. Mol. Biol.* 430:1386–1401. https://doi.org/10.1016/j.jmb.2018.02.018.
46. Maeda, R., H. Tamagaki-Asahina, …, Y. Sako. 2022. Threonine phosphorylation regulates the molecular assembly and signaling of EGFR in cooperation with membrane lipids. *J. Cell Sci.* 135, jcs260355. https://doi.org/10.1242/jcs.260355.
47. Masuyama, R., J. Vriens, …, G. Carmeliet. 2008. TRPV4-mediated calcium influx regulates terminal differentiation of osteoclasts. *Cell Metabol.* 8:257–265. https://doi.org/10.1016/j.cmet.2008.08.002.
48. Masuyama, R., A. Mizuno, …, T. Komori. 2012. Calcium/calmodulin-signaling supports TRPV4 activation in osteoclasts and regulates bone mass. *J. Bone Miner. Res.* 27:1708–1721. https://doi.org/10.1002/jbmr.1629.
49. Loukin, S., Z. Su, and C. Kung. 2011. Increased basal activity is a key determinant in the severity of human skeletal dysplasia caused by TRPV4 mutations. *PLoS One.* 6, e19533. https://doi.org/10.1371/journal.pone.0019533.
50. Kang, S. S., S. H. Shin, …, J. Chun. 2012. Human skeletal dysplasia caused by a constitutive activated transient receptor potential vanilloid 4 (TRPV4) cation channel mutation. *Exp. Mol. Med.* 44:707–722. https://doi.org/10.3858/emm.2012.44.12.080.
51. Ha, H., H. B. Kwak, …, H. H. Kim. 2003. Membrane rafts play a crucial role in receptor activator of nuclear factor kappaB signaling and osteoclast function. *J. Biol. Chem.* 278:18573–18580. https://doi.org/10.1074/jbc.M212626200.
52. Luegmayr, E., H. Glantschnig, …, A. A. Reszka. 2004. Osteoclast formation, survival and morphology are highly dependent on exogenous cholesterol/lipoproteins. *Cell Death Differ.* 11:S108–S118. https://doi.org/10.1038/sj.cdd.4401399.
53. Hada, N., M. Okayasu, …, Y. Hakeda. 2012. Receptor activator of NF-kappaB ligand-dependent expression of caveolin-1 in osteoclast precursors, and high dependency of osteoclastogenesis on exogenous lipoprotein. *Bone.* 50:226–236. https://doi.org/10.1016/j.bone.2011.10.028.
54. Okayasu, M., M. Nakayachi, …, Y. Hakeda. 2012. Low-density lipoprotein receptor deficiency causes impaired osteoclastogenesis and increased bone mass in mice because of defect in osteoclastic cell-cell fusion. *J. Biol. Chem.* 287:19229–19241. https://doi.org/10.1074/jbc.M111.323600.
55. Goswami, C., J. Kuhn, …, T. Hucho. 2010. Importance of non-selective cation channel TRPV4 interaction with cytoskeleton and their reciprocal regulations in cultured cells. *PLoS One.* 5, e11654. https://doi.org/10.1371/journal.pone.0011654.
56. Huai, J., Y. Zhang, …, S. W. Yue. 2012. Interaction of transient receptor potential vanilloid 4 with annexin A2 and tubulin beta 5. *Neurosci. Lett.* 512:22–27. https://doi.org/10.1016/j.neulet.2012.01.048.
57. Ayala-Sanmartin, J., J. P. Henry, and L. A. Pradel. 2001. Cholesterol regulates membrane binding and aggregation by annexin 2 at submicromolar Ca(2+) concentration. *Biochim. Biophys. Acta.* 1510:18–28. https://doi.org/10.1016/s0005-2736(00)00262-5.
58. Zobiack, N., U. Rescher, …, V. Gerke. 2002. Cell-surface attachment of pedestal-forming enteropathogenic E. coli induces a clustering of raft components and a recruitment of annexin 2. *J. Cell Sci.* 115 (Pt 1):91–98. https://doi.org/10.1242/jcs.115.1.91.
59. Illien, F., H. R. Piao, …, J. Ayala-Sanmartin. 2012. Lipid organization regulates annexin A2 Ca(2+)-sensitivity for membrane bridging and its modulator effects on membrane fluidity. *Biochim. Biophys. Acta.* 1818:2892–2900. https://doi.org/10.1016/j.bbamem.2012.07.012.
60. Varyukhina, S., A. Lamazière, …, J. Ayala-Sanmartin. 2022. The Ca(2+)- and phospholipid-binding protein Annexin A2 is able to increase and decrease plasma membrane order. *Biochim. Biophys. Acta Biomembr.* 1864, 183810. https://doi.org/10.1016/j.bbamem.2021.183810.
61. Zhang, Y., P. Liang, …, H. Yang. 2022. Functional coupling between TRPV4 channel and TMEM16F modulates human trophoblast fusion. *Elife.* 11, e78840. https://doi.org/10.7554/eLife.78840.
62. Das, A., J. L. Goldstein, …, A. Radhakrishnan. 2013. Use of mutant 125I-perfringolysin O to probe transport and organization of cholesterol in membranes of animal cells. *Proc. Natl. Acad. Sci. USA.* 110:10580–10585. https://doi.org/10.1073/pnas.1309273110.
63. Hotze, E. M., E. M. Wilson-Kubalek, …, R. K. Tweten. 2001. Arresting pore formation of a cholesterol-dependent cytolysin by disulfide trapping synchronizes the insertion of the transmembrane beta-sheet from a prepore intermediate. *J. Biol. Chem.* 276:8261–8268. https://doi.org/10.1074/jbc.M009865200.
64. Farrand, A. J., S. LaChapelle, …, R. K. Tweten. 2010. Only two amino acids are essential for cytolytic toxin recognition of cholesterol at the membrane surface. *Proc. Natl. Acad. Sci. USA.* 107:4341–4346. https://doi.org/10.1073/pnas.0911581107.
65. Rossjohn, J., S. C. Feil, …, M. W. Parker. 1997. Structure of a cholesterol-binding, thiol-activated cytolysin and a model of its membrane form. *Cell.* 89:685–692. https://doi.org/10.1016/s0092-8674(00)80251-2.
66. Ercan, B., T. Naito, …, Y. Saheki. 2021. Molecular basis of accessible plasma membrane cholesterol recognition by the GRAM domain of GRAMD1b. *EMBO J.* 40, e106524. https://doi.org/10.15252/embj.2020106524.
67. Das, A., M. S. Brown, …, A. Radhakrishnan. 2014. Three pools of plasma membrane cholesterol and their relation to cholesterol homeostasis. *Elife.* 3, e02882. https://doi.org/10.7554/eLife.02882.
68. Endapally, S., D. Frias, …, A. Radhakrishnan. 2019. Molecular Discrimination between Two Conformations of Sphingomyelin in Plasma Membranes. *Cell.* 176:1040–1053.e17. https://doi.org/10.1016/j.cell.2018.12.042.
69. Makino, A., M. Abe, …, T. Kobayashi. 2017. A novel sphingomyelin/cholesterol domain-specific probe reveals the dynamics of the membrane domains during virus release and in Niemann-Pick type C. *Faseb. J. : official publication of the Federation of American Societies for Experimental Biology.* 31:1301–1322. https://doi.org/10.1096/fj.201500075R.